GFZ

Helmholtz-Zentrum

POTSDAM

Accessory Phases from the Soultz monzogranite, Soultz-sous-Forêts, France: Implications for Titanite Destabilisation and Differential REE, Y and Th Mobility in Hydrothermal Systems

Alexander W. Middleton*[a], Hans-Jürgen Förster[b], I. Tonguç Uysal [a], Suzanne D. Golding [c] and Dieter Rhede[b]

[a] *Queensland Geothermal Energy Centre of Excellence, The University of Queensland, Queensland 4072, Australia*

[b] *Deutsches GeoForschungsZentrum GFZ, Telegrafenberg, D-14473 Potsdam, FR Germany*

[c] *School of Earth Science, The University of Queensland, Queensland 4072, Australia*

Abstract

The metaluminous Soultz-sous-Forêts monzogranite, France, is highly evolved and contains elevated concentrations of rare-earth elements (REE), Y and particularly Th. Primary accessory minerals include fluorapatite, allanite-(Ce) and Th-rich titanite. Primary titanite has been altered to anatase + calcite + quartz + synchysite-(Ce) ± bastnaesite-(Ce) or anatase + calcite + quartz + monazite-(Ce) + xenotime-(Y) ± thorite. Fluorocarbonate-bearing assemblages are restricted to those samples exhibiting minor selective alteration, whereas those containing phosphate-rich assemblages formed in pervasively altered samples that have experienced high fluid/rock ratios. Comparative electron-microprobe analysis of primary and hydrothermally-derived accessory phases found middle REE, Y and Th concentrations depleted in synchysite-(Ce) relative to primary titanite. Such depletions are not seen in phosphate-rich samples containing monazite-(Ce) and xenotime-(Y). Variability in elemental concentrations may be attributed to distinct fluid chemistries and hence, lead to differential mobility during alteration. Following previous experimental work and mineralogical observations, the ingress of CO_2-rich solutions was integral for titanite breakdown and the resultant metasomatic assemblage. The influx of CO_2-rich fluids concomitantly with

chloritisation of biotite produced fluids enriched in FCO_3^-. We, therefore, hypothesise that after the alteration of titanite, remnant HCO_3^- or FCO_3^--rich fluids were able to mobilise significant proportions of MREE, Y and Th not accommodated into the synchysite-(Ce) structure. Conversely, those samples rich in monazite-(Ce) and xenotime-(Y) retained their REE, Y and Th concentrations due to the presence of aqueous HPO_4^{2-} derived from apatite dissolution.

---

*Corresponding author Tel: +61 422708045

Email Address: alexander.middleton@uqconnect.edu.au

Keywords: Titanite; rare earth elements; Soultz-sous-Forêts; accessory phases; element mobility

1. Introduction

As part of the European Deep Geothermal Energy project, the Soultz-sous-Forêts monzogranite was drilled with the intention of establishing an Enhanced Geothermal System (EGS). The Soultz site received particular attention due to it representing a positive geothermal anomaly, arguably originating from convection cells of hot fluids within deeper basement and sediments (Aquilina et al., 1997). A notable characteristic of the Soultz monzogranite is the enrichment in heat-producing elements, particularly Th and U (Stussi et al., 2002). Uranium and Th commonly occur with rare earth elements and yttrium (REY) in primary accessory phases (Bea, 1996). The species of accessory phase is arguably dependent on the aluminosity (aluminium saturation index, ASI) of the igneous rock and may therefore vary from Ca-rich silicates (allanite and titanite) in metaluminous rocks (ASI <1), to Ca-poor

13 phosphates (monazite and xenotime) in peraluminous rocks (Cuney and Friedrich, 1987; Watt

14 and Harley, 1993; Wolf and London, 1994; Zen, 1986). Upon interaction with hydrothermal

15 fluids, primary accessory phases may destabilise and reprecipitate as polyminerallic alteration

16 assemblages. Analysis of these newly formed minerals is integral for understanding not only

17 the chemistry of the fluid, but also the mobility of constituent elements previously held in the

18 primary accessory phases.

19 This paper focuses on the metasomatic accessory phases of the Soultz monzogranite, with

20 specific attention to those formed by the breakdown of titanite. Previous studies established

21 that titanite may destabilise to: calcite + quartz + rutile ± REY-bearing phases including

22 allanite, bastnaesite $[LREE(CO_3)F]$, monazite $[LREEPO_4]$ and xenotime $[HREEPO_4]$

23 (Bancroft et al., 1987; Hunt and Kerrick, 1977; Pan et al., 1993). This study provides a

24 comprehensive analysis of the formation of the assemblage anatase + calcite + quartz +

25 LREE-rich synchysite $[(Ca,LREE)(CO_3)_2F]$ from alteration of titanite. Through electron-

26 microprobe studies of accessory species and ICP-MS analysis of their host rocks, we aim to

27 further understanding of REY mobility in hydrothermal solutions dominated by $F–CO_3^-$

28 complexation. Moreover, our contribution is of specific significance as it presents strong

29 evidence for hydrothermal Th mobility, conventionally considered an "immobile" element.

30

31 **2. Geological Setting**

32

33 The Soultz monzogranite is situated in the western district of the Rhine Graben, proximal to

34 the Vosges fault, and is overlain by Mesozoic to Cenozoic sedimentary cover (Stussi et al.,

35 2002). The sedimentary sequences comprise Cenozoic evaporites and claystones underlain by

36 Mesozoic limestones and sandstones; the latter forming the main aquifer for the region

37 (Aquilina et al., 1997). Borehole EPS1 was drilled in the monzogranite as part of European

38 investigations into EGS and exhibited elevated concentrations of radiogenic elements, K (~4

39   wt%), Th (24–35 ppm) and U (6–13 ppm) relative to upper continental crustal averages

40   (Hooijkaas et al., 2006). The enrichment in radiogenic elements as well as REY may be

41   related to assimilation–fractional crystallisation processes as postulated by Stussi et al.

42   (2002). Zircon U/Pb work by Alexandrov et al. (2001) dates the granite at 331 ± 9Ma

43   indicating a possible early Namurian emplacement (Gradstein and Ogg, 1997). The unaltered

44   post-metamorphic monzogranite is porphyritic, consisting of 1–8cm K-feldspar megacrysts in

45   a phaneritic matrix of quartz, plagioclase, biotite and hornblende, with primary accessory

46   fluorapatite, allanite, titanite, zircon and magnetite (Genter and Traineau, 1991).

47

48   The three most prominent alteration styles identified in the Soultz pluton are minor

49   "pervasive" propylitic, vein-related and weathering-related argillisation and formation of

50   haematite (Genter and Traineau, 1991; Ledésert et al., 2010). Although primary K-feldspar

51   and quartz appear unaltered, the primary ferromagnesian minerals (biotite and hornblende)

52   have undergone almost complete chloritisation, forming assemblages of chlorite + siderite +

53   opaques (haematite–magnetite) and chlorite + epidote (Genter and Traineau, 1991).

54   Plagioclase shows a similar intensity of selective alteration, forming needles of illite. Zones

55   proximal to fracture networks appear pervasively altered, with varying degrees of illitisation

56   and carbonatisation. In this study, we focus on the processes of pervasive alteration and its

57   chemical and mineralogical influence on the monzogranite.

58

59   **3. Analytical Techniques**

60   3.1 ICP-OES

61

62   For major-element analysis, samples were fused with lithium metaborate (~0.0500: 0.2000 g

63   sample/flux) in a Katanax Prime II automated fusion instrument. The samples were then

64   dissolved in 5% HNO_3 to a sample/solution weight ratio of 1: ~1000.

65   Total dissolved metals were determined using a Perkin Elmer Optima 8300 DV ICP-OES. All

66   reagents were prepared using double-distilled (sub-boiling) concentrated acids and Milli-Q

67   water (18.2 MΩ). All lab-ware was thoroughly cleaned by soaking in 1% Decon for 24 hr

68   then rinsed with high-purity water, followed by soaking in 5% HNO_3 for at least 48 hr, rinsed

69   several times with high-purity water and dried in HEPA filtered laminar flow cabinet before

70   use.

71

72   3.2 ICP-MS

73

74   For trace-element analysis, the samples were dissolved using $HF+HNO_3$ in Teflon beakers on

75   a hot plate. The dissolved samples were converted to nitrates and spiked with a multi-element

76   internal standard solution (^{6}Li, ^{61}Ni, ^{103}Rh, ^{115}In, ^{187}Re, ^{209}Bi, and ^{235}U) in 2% HNO3. Trace

77   elements were analysed by Inductively Coupled Plasma–Mass Spectrometry (ICP–MS) on a

78   Thermo X Series I. Sample preparation and analytical procedures used were similar to those

79   of Eggins et al. (1997), except that Tm was not used as an internal standard and duplicate

80   low-pressure digestions of W-2, a US Geological Survey diabase standard, were used as the

81   calibration standard. AGV1, AGV2 and G2 were run as unknown. The $^{156}CeO/^{140}Ce$ ratio for

82   the run was 0.016. Long-term precision (RSD) was based on duplicate analyses of the

83   duplicate digestions of AGV1, whilst precision for the run was based on five duplicate

84   analyses of W-2 which were better than 3% for most elements, except for Li, Zn, Mo, Cd,

85   and Cs, which ranged between 5% (Li, Cd and Cs) and 15% (Zn).

86

87   3.3 Electron-probe microanalysis

88

89   Electron-microprobe analyses of polished thin sections were performed in the wavelength-

90   dispersive mode using the JEOL JXA-8500F (Hyperprobe) at the Deutsches

91 GeoForschungsZentrum (GFZ) in Potsdam, Germany. Operating conditions involved an

92 accelerating voltage of 15 kV, a beam current depending on the minerals (5 nA for florencite,

93 7 nA for synchysite, 40 nA for monazite, xenotime and thorite and 60 nA for titanite and

94 allanite) and a variable beam diameter betweeen 1 and 10 μm, in order to minimise the

95 degradation of the sample surfaces. Kα lines were used for F, Mg, Al, Si, P, K, Ca, Ti, Mn

96 and Fe; Lα lines for Y, Nb, Zr, La, Ce, Yb and Lu; Lβ-lines for Pr, Nd, Sm, Gd, Tb, Dy, Ho,

97 Er; Mα-line for Th and Mβ-lines for Pb and U. Counting times on the peak were $30 - 100$ s

98 for the elements and, in each case, halftime for background counts on both sides of the peak.

99 X-ray lines and background offsets were selected to minimise interferences between elements

100 during analysis. Natural and synthetic minerals and synthetic REE+Y phosphates were used

101 as calibration standards. Matrix corrections were employed according to the Armstrong-

102 CITZAF method (Armstrong, 1995). Analytical errors were dependent not only on elemental

103 abundances in the analysed mineral phase, but also on the analytical conditions applicable to

104 the analysis of easily destructible mineral phases.

105

106 3.4 Micro-Raman spectroscopy

107

108 Raman spectra were recorded with a Jobin-Yvon LabRam HR800 spectrometer at the

109 Deutsches GeoForschungsZentrum, equipped with an Olympus optical microscope and a

110 long-working-distance LMPlanFI 100 x/0.80 objective. We used a 488 nm excitation of a

111 Coherent Ar+ laser Model Innova 70°C, a power of 300 mW (about 14 mW on sample), at a

112 resolution of ≤ 0.6 cm^{-1}. Each unpolarized spectrum represents the accumulation of six

113 acquisitions of 20 s each. The spectra were collected at a constant laboratory temperature

114 (20°C) with a Peltier-cooled CCD detector, and the positions of the Raman bands were

115 controlled and eventually corrected using the principal plasma lines in the Argon laser. The

116 divergence between the recommended and measured positions of the plasma lines in the

117 fingerprint spectral region is not larger than 0.6 cm^{-1}.

118

119

120 **4. Results**

121

122 4.1 Sample Description

123

124 *4.1.1 K102 (1,608m depth)*

125

126 The shallowest of the samples, K102 represents the least altered specimen of the Soultz

127 monzogranite studied in this paper. Alteration of major phases is restricted to minor selective

128 illitisation of plagioclase and partial chloritisation of biotite, with secondary intercleavage-

129 grown anhedral titanite. Minor hornblende has been altered to epidote.

130

131 Primary accessory phases, titanite and allanite, are largely unaltered. Allanite, however,

132 shows compositional variation in back-scattered electron (BSE) images, indicating localised

133 epidotisation with consequent element mobilisation (Fig. 1a). Titanite commonly contains

134 inclusions of magnetite, zircon and fluorapatite, with the foremost being partially replaced by

135 ilmenite. Fractured titanite grains have also experienced localised minor alteration to allanite

136 (Fig. 1b).

137

138

139 *4.1.2 K108 (1,629m depth)*

140

141 K108 is semi-pervasively altered, with multiple generations of cross-cutting illite and *quartz*

142 *+ ankerite ± synchysite veinlets*. Tabular, zoned synchysite grains occur within Mn-rich

143 cores of the oscillatory-zoned ankerite. With the exception of a K-feldspar-shielded

144 polyminerallic titanite-pseudomorph assemblage (PPA) of anatase + ankerite + quartz +

145 synchysite–(Ce) + monazite-(Ce) ± zircon, the remaining PPAs contain *anatase + calcite +*

146 *quartz + monazite-(Ce) + xenotime-(Y)*. Xenotime-(Y) is frequently external from the PPA,

147 rimming nearby zircons. Primary fluorapatite has been significantly altered and no longer

148 occurs as oscillatory-zoned, euhedral crystals, but rather as almost completely anhedral

149 grains. Major mineral phases plagioclase and biotite have been almost entirely illitised and

150 carbonatised, whereas K-feldspar remained unaffected apart from sporadically occurring

151 anhedral barite inclusions.

152

153

154 *4.1.3 K177 (2,061m depth)*

155

156 K177 has been selectively altered, with complete chloritisation of hornblende and biotite and

157 illitisation of plagioclase. Chloritised biotite also includes presents intercleavage-grown

158 secondary ankerite. Fe-stained K-feldspar commonly hosts secondary barite, carbonate

159 microveins and altered titanite. Titanite grains vary from unaltered, oscillatory-zoned

160 euhedral crystals to highly altered, forming voids hosting PPAs. Altered titanite is present as

161 either "dusted-opaque" rhombs or as euhedral-subhedral alteration pseudomorphs. Subhedral

162 pseudomorphs were identified as largely anatase, with supporting quartz–carbonate matrix.

163 Energy dispersive X-ray spectroscopy (EDS) and microRaman showed the assemblage to be

164 *anatase + calcite + quartz + synchysite-(Ce) ± bastnaesite-(Ce)* (Fig. 1b). Back-scattered

165 images identify two varieties of PPA, where synchysite-(Ce) formed highly birefringent,

166 tabular crystals (including isolated "spongy" grains) or acicular needles. The acicular needles

167 are concentrated in titanite voids bordered by chlorite and quartz, whereas tabular phases

168 rimmed voids within K-feldspar grains. Small synchysite grains proved difficult to analyse as

169 samples were readily decomposed under a focused electron beam. Those appropriate for

170 microprobe analysis were 15–50 by 10–40μm grains. The occurrence of bastnaesite is limited

171 and was only identified in one titanite-derived PPA.

172

173 Fluorapatite grains suffered minimal alteration to monazite-(Ce) (Fig. 3a + b) and rarely

174 synchysite-(Ce), consistently found in REE-depleted domains, which appear dark in BSE

175 image. Allanite-(Ce) has been completely replaced by calcite + illite + anatase + quartz +

176 synchysite-(Ce) + bastnaesite-(Ce) + thorite (Fig. 4a + b). Allanite-(Ce), however, has a

177 fractured appearance, with minor bastnaesite-(Ce) flakes within synchysite-(Ce) masses.

178

179 Although an isolated example, the assemblage: Nb-rich anatase + rutherfordine(?)

180 $[UO_2(CO_3)]$ + quartz + illite were found pseudomorphing the void of supposed

181 uranopolycrase $[(U,Y)(Ti,Nb,Ta)_2O_6]$ (Fig. 5). Euhedral Nb-rich anatase crystals occur

182 inwardly rimming the uranopolycrase void, whereas anhedral grains are fracture-grown and

183 coated with rutherfordine needles.

184 ,

185 *4.1.4 K206 (2,216m depth)*

186

187 K206 has experienced the most pervasively destructive form of hydrothermal alteration,

188 which comprises kaolinitisation ± silicification overprinted by carbonatisation and illitisation

189 followed by late-stage haematisation. Plagioclase is almost entirely kaolinitised and illitised,

190 with minimal internal structure preserved, whereas K-feldspar appears insignificantly

191 affected by alteration. Very few remnant fluorapatite grains were identified in thin section.

192 Those remaining appear as anhedral grains with invasive illite veinlets (Fig. 6). Despite the

193   abundance of illite ± anatase ± zircon veinlets, sparse grains of chloritised biotite are

194   observed in the sample. Illite veins are occasionally bordered by small grains of a LREE-rich

195   aluminophosphate, tentatively identified by WDS-EMPA as Sr-rich intermediate florencite-

196   (La)–florencite-(Ce) solid solutions, $(La,Ce)Al_3(PO4)_2(OH)_6$. Unlike K108, K206 has no

197   recognisable synchysite grains within or surrounding decomposed titanite. The PPAs are

198   composed of ***anatase + calcite + quartz + monazite-(Ce) + xenotime-(Y) ± thorite*** (Fig. 7a +

199   b). Monazite-(Ce) and xenotime-(Y) represent the major REE-bearing phases.

200

201

202   4.2 Whole-rock geochemistry

203

204   The samples studied in this paper all refer to the same textural variant of the granite and, thus,

205   should have approximately the same primary geochemistry. In order to validate this

206   assumption, Ti concentrations were determined for the analysed samples. In granitic rocks, Ti

207   is documented to be the most resistant element against alteration (Förster et al., 1999) so will,

208   therefore, mirror primary element variation. The fact that all samples display virtually the

209   same Ti concentrations (Table 1), supports the conclusion of being derived from the same

210   progenitor. Consequently, the bulk of major and trace element variation recognized in the

211   samples should be alteration-induced.

212

213   With the exception of an anomalous kink for Ce_{CN}, all samples appear to have similar

214   gradients for chondrite-normalised REY patterns (Fig. 8a) from La_{CN} to Eu_{CN}. Despite similar

215   LREE patterns, K108 and K177 show elevated concentrations of LREE (La/Dy of 19.5 and

216   27.3, respectively) compared to K102 and K206 (La/Dy of 15.0 and 15.9, respectively).

217   Samples K102, K108 and K208 have near identical REY patterns between Gd_{CN} and Lu_{CN}

218   whereas K177 steepens significantly from Gd_{CN} until Y_{CN} where it plateaus out to Lu_{CN}. This

219   is further indicated by similar Dy/Lu values for K102, K108 and K206 compared to K177

220   (Table 1). Total REY contents vary from 204 ppm (K102) to 408 ppm (K177). Thorium

221   content is highly variable and shows two populations: those samples containing (REY, Th)–

222   fluorocarbonates, which are rich in Th (K108 – 59.6 ppm and K177 – 67.0); and relatively

223   Th-poor samples (K102 – 23.7 and K206 – 24.2) that are devoid of fluorocarbonates

224

225   4.3 Mineral compositions

226

227   *4.3.1 Primary minerals*

228

229   *Titanite*

230

231   Compositionally, titanite can be grouped according to variations in the concentration of REY

232   and Th (Table 2). REY-rich domains (average total REY_2O_3 3.7 wt%) coincide with bright

233   BSE zones and poor domains with dark BSE zones (average total REY_2O_3 1.3 wt%). Bright

234   zones are dominated by LREE plus Y, with average concentrations (in wt%) of 0.33, 0.48,

235   1.55 and 0.72 for Y_2O_3, La_2O_3, Ce_2O_3 and Nd_2O_3 respectively. Thorium concentrations vary

236   between 0.05 and 0.15 wt% ThO_2. Those domains poorer in REY contain relatively elevated

237   contents of Nb (0.62 wt% Nb_2O_5) and Al (1.58 Wt% Al_2O_3), reflecting the coupled

238   substitution reaction $Nb^{5+} + Al^{3+} \Leftrightarrow 2Ti^{4+}$, whereas those rich in REY have lower average Nb

239   (0.49 wt% Nb_2O_5) and Al (1.32 wt% Al_2O_3). Chondrite-normalised REY patterns (Fig. 8b)

240   are relatively flat, with only minor relative enrichment in LREE as seen by the average

241   La_{CN}/Dy_{CN} and La_{CN}/Nd_{CN} ratios, 7.4 (dark) to 9.8 (bright) and 1.9 (dark) to 1.3 (bright),

242   respectively. Accurate HREE concentrations were not acquirable as they were at or below

243   detection limit for the methods employed.

244

245

246 *Allanite-(Ce)*

247

248 Like titanite, allanite-(Ce) grains possess bright and dark BSE regions of distinct chemistries

249 (Fig. 8b). The variation in brightness in BSE is, however, unrelated to growth zonation and

250 can be attributed to the epidotisation of the rim and fractures (Figure 1a).

251

252 Where bright BSE regions have concentrations of 1.4, 9.6 and 10.1 wt% for ThO_2, La_2O_3 and

253 Ce_2O_3 respectively, altered dark regions are relatively depleted in these, with 0.7, 4.7 and 4.6

254 wt%, respectively (Table 2). This is seen in the total REY_2O_3 concentrations as bright

255 allanite-(Ce) (21.3 wt%) has approximately twice the REY_2O_3 as the dark allanite-(Ce) (10.0

256 wt%). Conversely, altered allanite-(Ce) contains elevated concentrations of Ca (17.5 wt%

257 CaO), Al (19.3 wt% Al_2O_3) and Si (35.3 wt% SiO_2) compared to unaltered allanite with 11.8,

258 12.7 and 32.0 wt%, respectively. The average La_{CN}/Dy_{CN} and La_{CN}/Nd_{CN} ratios vary from

259 300 (dark) to 980 (bright) and 19.4 (dark) to 16.2 (bright), respectively, indicating a

260 significant enrichment in LREE to MREE.

261

262 *Thorite*

263

264 Thorite occurs as both a primary and secondary phase. Metasomatic grains are too small to

265 permit acquisition of accurate analytical data and are only located within previous mineral

266 voids as part of PPAs. Magmatic thorite grains are partially fractured, with minimal evidence

267 of dissolution along the rim and are found as isolated phases in the rock matrix. Of the

268 analysed thorite, grains from K206 and K108 provided two chemical populations respectively

269 (Fig. 8c); those richer in LREE (av. La_{CN}/Yb_{CN} of 2.2) from K206 and those poorer in LREE

270 (av. La_{CN}/Yb_{CN} of 0.4) from K108. This discrepancy is principally dictated by the

271 concentrations of La_2O_3, Ce_2O_3 and Pr_2O_3 as seen from the proportionally elevated values of

272 $\Sigma La_2O_3-Pr_2O_3$ for K206 (av. 1.63 wt%) to K108 (av. 0.37 wt%). Uranium and Th

273 concentrations vary only slightly between the two chemical populations: 6.2 UO_2 and 60.5

274 wt% ThO_2 (K206) and 4.6 UO_2 and 62.9 wt% ThO_2 (K108) respectively (Table 3).

275

276 *4.3.2 Secondary Minerals*

277 *K177 - Bastnaesite-(Ce)*

278

279 Only one grain of bastnaesite from a partially dissolved grain of allanite-(Ce) was appropriate

280 for analysis owing to grain-size restrictions and grain morphology (Table 4). As such its

281 chondrite-normalised REY pattern from La–Nd is almost identical in gradient to primary

282 allanite but is, however, similar in gradient to synchysite-(Ce) patterns from Sm–Yb (e.g.,

283 Fig. 8d). The steep La–Nd pattern is exemplified by the larger La_{CN}/Dy_{CN} ratio of 128 as well

284 as a La_{CN}/Nd_{CN} ratio (15) similar in value to allanite–(Ce). The dominant cations of

285 bastnaesite-(Ce) are (in descending order): Ce (32.6 wt% Ce_2O_3), La (29.6 wt% La_2O_3), Nd

286 (3.9 wt% Nd_2O_3) and Pr (1.8 wt% Pr_2O_3), respectively. As to nomenclature, the analysed

287 grain represents an intermediate bastnaesite-(Ce)–bastnaesite-(La) solid solution.

288

289 *K177 – Synchysite-(Ce)*

290

291 Synchysite appears relatively homogenous under high contrast BSE imaging. However, many

292 grains analysed with microRaman contain nano-scale anatase inclusions as seen from the

293 Raman shift (Fig 9a). Apparent anatase peaks were cross-referenced with those from pure

294 anatase found in PPAs (Fig.9b). Synchysite-(Ce)–anatase spectra were acquired from grains

295 within or rimming the titanite void. Although very few examples were present, grains

296 relatively distal to the PPA display little to no anatase spectra (Fig. 9c) inferring the absence

297 of inclusions.

298

299 Synchysite-(Ce) stoichiometry indicates an occasional minor excess of Ti, Ca and/or Si,

300 reflecting the presence of nano-scale inclusions of anatase, calcite and quartz that were not

301 visible in BSE image. In addition to Ca (16.5–17.9 wt% CaO), the prevalent cations in

302 competent synchysite-(Ce) grains are (in descending order as oxides): Ce (20.9–25.5 wt%),

303 La (7.8–14.22 wt%), Nd (5.6–11.9 wt%), Y (0.9–2.6 wt%) and Pr (1.9–3.1 wt%) (Table 4).

304 The variation in cation content is related to the grain surface-texture. Those grains with

305 higher Th, Y, Pr and Nd concentrations are "spongy" in appearance compared to those with

306 relatively elevated La and Ce. Chondrite-normalised REY diagrams show a flat to slight

307 inclination from La–Nd (Fig. 8d), with a moderate decrease in value and steepening slope

308 from Sm–Yb, excluding Y. This is seen from La_{CN}/Dy_{CN} and La_{CN}/Nd_{CN} ratios averaging to

309 31.5 and 2.3, respectively. The REE pattern of synchysite-(Ce) from La–Nd appears almost

310 identical to that of titanite. Yttrium presents a positive anomaly in REY plots showing an

311 average Dy_{CN}/Y_{CN} value of 1.07. The highest La (14.2 wt% La_2O_3) and Ce (25.5 wt% Ce_2O_3)

312 contents coincide with the lowest Nd (5.6 wt% Nd_2O_3) possessed by a synchysite-(Ce) grain

313 within a dark apatite embayment. Its location within fluorapatite explains the different

314 composition of this synchysite–(Ce) relative to that crystallized in titanite PPAs. Thorium

315 content ranges from 0.0–2.1 wt% ThO_2, the larger indicating "spongy" grains.

316

317 *K108 and K206 – Monazite-(Ce)*

318

319 Element concentrations vary only slightly (Table 5) with the exception of one grain of

320 monazite from destabilised allanite (Fig. 8e – circle). This anomalous grain has La_2O_3,

321 Ce_2O_3, Pr_2O_3, Nd_2O_3 and La_{CN}/Nd_{CN} of 28.5 wt%, 31.4 wt%, 1.75 wt%, 3.9 wt% and 7.1,

322 respectively, thus representing an intermediate solid solution of monazite-(Ce) and monazite-

323 (La). The remaining grains form two chemically distinct groups, representing monazites

324 formed from apatite dissolution (Fig. 8e– square) and those from titanite dissolution (Fig. 8e

325 – triangle). The former are characterised by La_2O_3, Ce_2O_3, Nd_2O_3, La_{CN}/Nd_{CN} and La_{CN}/Dy_{CN}

326 of 18.8–21.9 wt%, 33.1–34.1 wt%, 7.4–9.1 wt%, 4.0–5.6 and 222–1110, whereas the latter

327 have concentrations of 9.8–15.8 wt%, 31.1–34.8 wt%, 9.5-15.5 wt%, 1.2–2.8 and 37.2–127,

328 respectively. Chondrite-normalised REY diagrams of monazite-(Ce) with lower La_{CN}/Dy_{CN}

329 have LREE patterns similar to primary titanite, however, steepen significantly from Sm–Yb,

330 with negative Y anomalies of av. 3.9 (Dy_{CN}/Y_{CN}). The chondrite-normalised REY patterns of

331 monazite-(Ce) from dissolved fluorapatite have regular and moderately steep gradients from

332 La–Nd, with similar steepening (to above) from Sm–Yb and Dy_{CN}/Y_{CN} (3.8). The anomalous

333 grain chondrite-normalised REY pattern is similar to previously analysed allanite grains and

334 has a steep gradient from La–Nd, with significant steepening from Sm onwards.

335

336 *K108 and K206 – Xenotime-(Y)*

337 Yttrium concentrations vary from 41.9–42.4 wt% Y_2O_3, with an average value of 42.2 wt%

338 for both samples. As LREE are less readily incorporated into the xenotime structure,

339 concentrations of Ce (0.04–0.06 wt% Ce_2O_3), Pr (0.07–0.1 wt% Pr_2O_3) and Nd (0.4–0.7 wt%

340 Nd_2O_3) content are low. As such, chondrite-normalised REY diagrams (Fig. 8f) have steep

341 positive gradients from Ce–Sm but plateau significantly from Gd–Lu. The only noticeable

342 variation in chondrite-normalised HREE is seen from a divergence of patterns after Er_{CN}

343 [Er_{CN}/Lu_{CN} 1.1 (K108) and 1.7 (K206)]. Thorium concentrations vary from 0.16 to 0.26 wt%

344 ThO_2 and 1.09 to 1.14 wt% ThO_2 for K108 and K206, respectively (Table 6).

345

346

347 **5. Discussion**

348

349 SEM and EPMA results indicate that titanite has undergone destabilisation and resulted in two

350 end-member metasomatic assemblages. These assemblages are typified by REE, Y and Th-

351 bearing fluorocarbonates in K177 (CO_2–F) or phosphates plus silicates in K108 and K206

352 (CO_2–HPO_4^{2-}). The variation in mineralogy stems from differing chemistries of alteration

353 fluids and variable fluid/rock ratios. In the following section we attempt to evolve genetic

354 models for CO_2–F and CO_2–HPO_4^{2-}-dominated alteration; with specific attention to titanite

355 destabilisation and REY and Th mobility.

356

357 *5.1 Source of REY and Th in secondary accessory phases*

358

359 In the metaluminous (ASI <1) and Ca-rich (~2 wt% CaO) monzogranite at Soultz, titanite,

360 allanite-(Ce), fluorapatite and minor thorite constitute the principle carriers of REY and Th

361 (Stussi et al., 2002). From these magmatic species, titanite is the precursor of the

362 pseudomorph assemblages observed in samples K108, K177 and K206. This is further

363 substantiated by REY and Th-bearing fluorocarbonate and phosphate grains within or

364 rimming titanite voids as well as almost identical REY patterns for titanite, synchysite-(Ce),

365 and monazite-(Ce).

366

367 Comparison of bulk-rock data, mineral EPMA data and La_{CN}/Nd_{CN} ratios (Ttn: 1.3, Syn: 2.3

368 and Mon: 2.1) indicates relative enrichment of synchysite-(Ce) and monazite-(Ce) in La and

369 Ce relative to titanite. This implies an additional source, richer in these LREE than titanite,

370 such as allanite-(Ce) or LREE-rich uranopolycrase. Use of La_{CN}/Nd_{CN} ratios is justified on the

371 basis of uniform Nd wt% of ΣREY for titanite, synchysite-(Ce) and monazite-(Ce). Elevated

372 concentrations of LREE in allanite (Fig 8a) can be traced to the timing of crystallisation

373 (Gromet and Silver, 1983), with titanite forming first, producing relative depletion in HREE

374 in the melt, allowing a now LREE-rich allanite-(Ce) to crystallise.

375

376 Fluorapatite may also constitute a potential carrier of REE and high-field strength elements

377 (HFSE) in metaluminous granites (Watt and Harley, 1993). In sample K177, quartz-shielded

378 euhedral fluorapatite displays minimal evidence of dissolution. Primary fluorapatite grains

379 with minor dissolution–reprecipitation structures generally contain monazite-(Ce) or

380 synchysite-(Ce) within voids, indicating minimal if any release of REE into the hydrothermal

381 fluid (cf. Harlov et al., 2005). Moreover, those components released into solution are unlikely

382 to have been mobilised significant distances due to the presence of Ca^{2+} (Salvi and William-

383 Jones, 1996), a common cationic ligand destabiliser of REE and HFSE that have complexed

384 with bi-ligands such as FCO_3^- or HCO_3^- (Wood, 1990b).

385

386 A different situation is observed in samples K108 and K206, where texturally destructive

387 alteration resulted in almost complete dissolution of fluorapatite and allanite-(Ce). Due to the

388 degree of alteration, it is difficult to assess the full contribution of these phases to the aqueous

389 REY and Th budget. The discovery of hydrothermal monazite-(Ce) grains deriving from

390 allanite-(Ce) and fluorapatite, however, imply an active input of REY and Th to the

391 hydrothermal solution. Grains of primary thorite appear minimally, if at all, altered and are

392 therefore discounted as potential REY and Th sources.

393

394

395 5.2 CO_2–F_2-dominated alteration

396

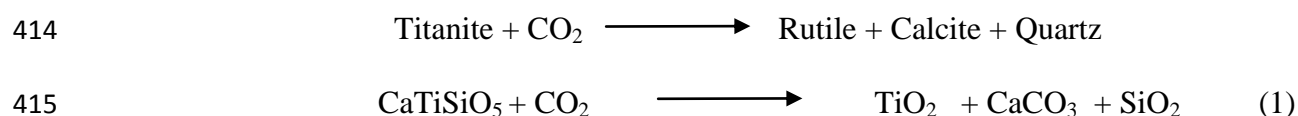397 *5.2.1 Origin and role of volatiles*

398

399   The occurrence of contemporaneous synchysite-(Ce) and ankerite indicates the presence of

400   CO_2 in the metasomatising fluid (Förster, 2001). Moreover, fluid inclusion (FI) studies by

401   Dubois *et al.* (1996) of carbonate–quartz veins from EPS1–2052.1 m (10 m above K177)

402   detected CO_2-rich solutions within isolated and euhedral quartz FI clusters, with

403   homogenisation temperature–pressure pairs of ~350°C/~2.2kbar and 295°C/0.6kbar,

404   respectively. These fluids may be sourced from either pressure and crystallisation-related

405   degassing of deeper mafic enclaves (Lowenstern, 2001; Stussi et al., 2002) or from an influx

406   of meteoric water that has interacted with carbonate/organic-rich sedimentary units (Fouillac

407   and Genter, 1992).

408

409   The ingress of CO_2-rich solution would have been integral for both carbonate formation and

410   titanite destabilisation (Corlett and McIlreath, 1974; Hunt and Kerrick, 1977; William-Jones,

411   1981). In this context, Hunt and Kerrick (1977) found that at 0.5 XCO_2, <500°C and 2kbar,

412   titanite will destabilise according to the following equation:

413

414   Titanite + CO_2 $\longrightarrow$ Rutile + Calcite + Quartz

415                $CaTiSiO_5 + CO_2$ $\longrightarrow$ $TiO_2 + CaCO_3 + SiO_2$ (1)

416

417   This equation, however, involves an idealised composition of titanite not matching the actual

418   composition of this species in most igneous bodies, especially evolved felsic granites

419   exemplified by the Soultz monzogranite (Stussi et al., 2002; Xie et al., 2010). Taking into

420   account the mineralogy at Soultz, as well as notably similar geochemical occurrences reported

421   by Pan et al. (1993), the following reaction is more applicable:

422

423   Titanite + CO_2 + F_2 + H_2O $\longrightarrow$ Anatase + Calcite + Quartz + Synchysite ± Bastnaesite

424

425     $2(Ca, REE, Ti, Th)SiO_5 + 3.5CO_2 + 0.75F_2 + 1.5H_2O \longrightarrow$

426     $2TiO_2 + CaCO_3 + 2SiO_2 + (Ca, REE, Th)(CO_3)_2F \pm 0.5(REE, Th)(CO_3)F + 0.5Th^{4+} +$
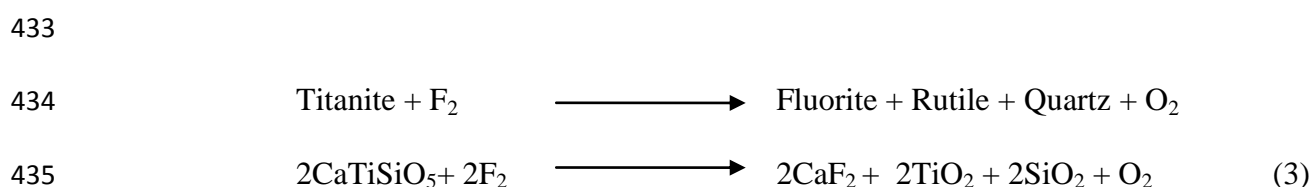
427     $0.5REE^{3+} + 3H^+$ (2)

428
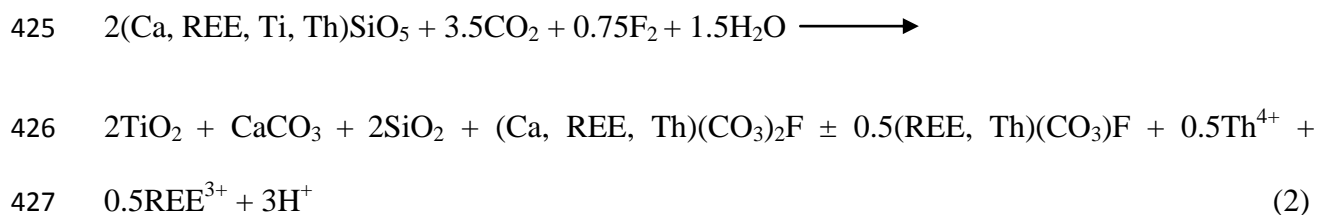
429   Fluorine in isolation has also been noted to promote the breakdown of titanite (Bohlen and

430   Essene, 1978; Troitzsch and Ellis, 2002). The resultant assemblage presented by Bohlen and

431   Essene (1978) idealised that, under low fluorine and moderate oxygen fugacities, titanite is

432   decomposed by the reaction:

433

434          $Titanite + F_2 \longrightarrow Fluorite + Rutile + Quartz + O_2$

435          $2CaTiSiO_5 + 2F_2 \longrightarrow 2CaF_2 + 2TiO_2 + 2SiO_2 + O_2$ (3)

436

437   This reaction is unlikely to have operated at Soultz as seen by the lack of fluorite (CaF_2) in

438   PPAs. However, formation of synchysite-(Ce) unambiguously demonstrates that F played an

439   essential role during alteration. The most likely source of fluorine can be traced to the anionic

440   loss during chloritisation of biotite (Simon, 1990; Förster, 2000).

441

442

443   *5.2.2 REY and Th mobility*

444

445   Relative elemental abundances of selected elements (La, Dy, Y and Th) were calculated in

446   order to determine element behaviour/mobility during alteration and mineral formation.

447   Element comparison graphs were produced for La, Dy and Y by plotting chosen element

448   percentages (of the total REY wt.%) against ΣREY wt.% in synchysite, monazite, xenotime

449   and thorite. La and Dy were chosen to act as proxies for light and middle REE, respectively.

450   Thorium comparison graphs differ only with the addition of Th to total REY wt.% values.

451   These graphs do not constitute absolute mass-balance calculations as total modal mineral

452   percentages and accurate mineral volume is unknown.

453

454   Rare-earth elements and Y can be variably mobilised by hydrothermal fluids depending on a

455   number of geochemical parameters such as pH, composition and redox conditions (Bau, 1991;

456   Uysal et al., 2011; Wood, 1990a; Wood, 1990b). As seen from Fig. 10a, there is a substantial

457   increase in the percentage of La of ΣREY from "parental" titanite to synchysite-(Ce),

458   suggesting involvement of a LREE-rich hydrothermal fluid. This is further substantiated by an

459   elevated LREE content in K177 relative to unaltered K102 (Table 1). The enrichment in

460   LREE may originate from intense alteration and leaching from areas proximal to K177 by

461   fluids rich in FCO_3^- or HCO_3^-. Evidence of this phenomenon was noted by Stussi et al. (2002)

462   from bulk-rock analysis of K178 (from the same core) that had significantly depleted REE

463   concentrations. An alternative hypothesis arises from REE separation by preferential sorption.

464   Assuming a mildly acidic pH (Bau and Möller, 1991; Sanematsu et al., 2011), hydrothermal

465   fluids may be depleted in HREE as their sorption strength is higher than that of their lighter

466   counterparts in the presence of certain sheet silicates allowing preferential LREE mobilisation

467   in the aqueous phase (Coppin et al., 2002). Since CO_2 is present in the system, acidity is

468   inferred from the formation of carbonic acid (Barclay and Worden, 2000) and may therefore

469   allow REE transportation with differential separation by sorption, hence enriching the newly

470   forming synchysite-(Ce) in La.

471

472   Following breakdown of titanite, REY and Th were held in aqueous phase via speciation by

473   soft ligands (Bau, 1991; Bau and Möller, 1991) such as (bi)carbonate or fluorocarbonate

474   complexes (Förster, 2000; Wood, 1990a; Wood, 1990b) as indicated by the presence of

475   synchysite-(Ce) and bastnasite-(Ce). These species would prevail over ligand F^- complexes

476   (Wood, 1990b) as the abundance of free fluorine would have triggered the precipitation of

477   fluorine-bearing phases such as fluorite (Förster, 2001). As most synchysite-(Ce) grains form

478   part of a pseudomorph or are proximal to the attributing PPA, the distance of transport for

479   those incorporated elements was minimal. The apparent immobility is, however, expected as

480   the strong affinity of calcium for CO_3^{2-} and F^- will buffer the concentration of ligands

481   available for complexation through mineral precipitation (Salvi and William-Jones, 1990;

482   Salvi and William-Jones, 1996). The MREE, Y (MREE + Y, MREY) and Th on the other

483   hand show an increased mobility as seen by the depletion of Dy, Y and Th in synchysite-(Ce)

484   relative to precursor titanite (Fig 10b – d). The loss of MREY and Th may be attributed not

485   only to the preferential incorporation of LREE into the synchysite-(Ce) crystal structure

486   (Förster, 2000; Förster, 2001; Wang et al., 1994), but also the comparatively higher stability

487   constants for MREE (Wood, 1990b) with mobilising ligands. The particularly large depletion

488   in Y may indicate that in the presence of bi-ligand complexes such as fluorocarbonates, it will

489   act as a more mobile "heavy pseudolanthanide" (Bau and Dulski, 1995). The term "heavy

490   pseudolanthanide", in this instance, refers to the ability of Y to act in a similar manner to

491   HREE (Ho to Lu) in solution. As such, this phenomenon may offer a potential explanation for

492   the relative depletion in HREE of K177 compared to K102. The paucity of Th in synchysite-

493   (Ce) from Soultz, and therefore increased mobility of Th in solution, is potentially the

494   combined result of the lack of accommodation space in the newly formed phase resulting

495   from La and Ce abundance, and the availability of residual FCO_3^- or HCO_3^- to mobilise the

496   Th away from the site of titanite breakdown. The availability of such mobilising bi-ligands

497   may also be the cause of the substantial enrichment of K177 in Th relative to unaltered K102

498   (Table 1). This finding may therefore imply the extent of Th mobilisation is significantly

499   increased in hydrothermal environments dominated by FCO_3^- and HCO_3^- with moderate

500   fluid-rock ratio conditions.

501

502

503   5.3 CO_2–HPO_4^{2-} -dominated alteration

504

505   *5.3.1 Origin and role of volatiles*

506

507   With the exception of an isolated synchysite-(Ce) grain in K108, secondary monazite-(Ce)

508   and xenotime-(Y) are the principle REY reservoirs in pervasively altered K108 and K206. As

509   these samples have virtually no euhedral apatite, it is likely that destabilised fluorapatite was

510   the major source of aqueous phosphate for monazite-(Ce) and xenotime-(Y) precipitation.

511   Experimental work by Harlov and Förster (2003) and Harlov et al. (2005) demonstrated that

512   apatite will readily destabilise through interaction with KCl, HCl and H_2SO_4-dominated

513   solutions, with dissolution–reprecipitation reactions forming REE phosphate inclusions.

514   Following the work of Pan and Fleet (2002), monazite-(Ce) precipitation can result to

515   compensate for charge imbalance following the original coupled substitution shown below:

516

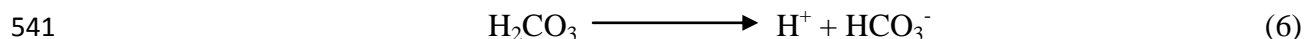517 $Si^{4+} + (Y+REE)^{3+} \longrightarrow P^{5+} + Ca^{2+}$ (4)

518   and

519                    $Na^{+} + (Y+REE)^{3+} \longrightarrow 2Ca^{2+}$ (5)

520

521   During dissolution of (Y+REE)-rich apatite , preferential loss of Na^{2+} and Si^{4+} results in a

522   charge imbalance allowing the precipitation of monazite/xenotime in (Y+REE)-poor embayed

523   apatite (Harlov et al., 2002). Examples of nano-channel (Harlov et al., 2005) alteration are

524   limited to sample K177, where tiny monazite and rarely synchysite grains are present in the

525   majority of fluorapatite grains (Fig. 3a + b). Nano-channels can be defined as "groups of

526   parallel, 5–20 nm wide, hollow, irregular trails of interconnected nano-voids" that may serve

527   as nucleation sites for monazite following apatite dissolution (Harlov et al., 2005). Although

528   apatite breakdown may be caused by the introduction of HCl/H_2SO_4 (Harlov et al., 2005), it is

529   more likely that low-pH KCl-rich brines contributed, with consequent pervasive sericitisation

530   and zircon−anatase-rich illite veining (Bonyadi et al., 2011; Giére, 1990; Torab and Lehmann,

531   2007). The influx of aqueous brines is further postulated from previous fluid-inclusion studies

532   (Dubois et al., 1996) as well as onsite water sampling (Aquilina et al., 1997; Pauwels et al.,

533   1993).

534

535   The ingress of KCl-rich fluid, however, does not account for extensive PO_4^{3-} in solution but

536   rather implies immediate precipitation of REE-bearing phosphates in and adjacent to zones of

537   metasomatised fluorapatite. An alternative possibility is that fluorapatite dissolution occurred

538   under near neutral conditions, as a result of carbonic acid dissociation from CO_2-rich fluids at

539   a late stage of the fluid-rock interaction process (Eq. 6) (Harouiya et al., 2007) :

540

541    $$H_2CO_3 \longrightarrow H^+ + HCO_3^- \tag{6}$$

542

543    $$Ca_5(PO_4)_3F + 3H^+ \longrightarrow 5Ca^{2+} + 3HPO_4^{2-} + F^- \tag{7}$$
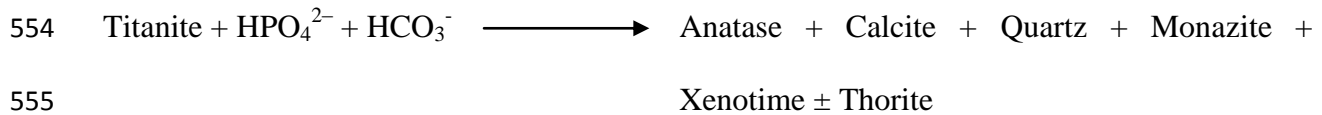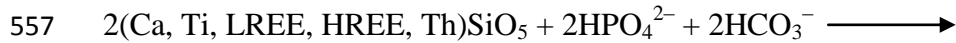
544

545

546   Due to pervasive illitisation and carbonatisation, one can assume both KCl- and CO_2-rich

547   fluids played active roles during alteration (Bonyadi et al., 2011). Determination of fluid

548   succession from cross-cutting relations has, however, proven impossible due to several stages

549   of overprinting. This may indicate mixing of CO_2-rich fluids with KCl-rich basinal brines of

550   the Permian Bundsandstein Formation (Kominou and Yardley, 1997). Upon interaction with

551   K–Cl–CO_2-rich solutions, dissociated carbonic acid would have resulted in apatite breakdown

552   (Eq. 7) and subsequent titanite dissolution (Bancroft et al., 1987) :

553

554         $\text{Titanite} + HPO_4^{2-} + HCO_3^{-} \longrightarrow \text{Anatase + Calcite + Quartz + Monazite +}$

555 $\text{Xenotime} \pm \text{Thorite}$

556

557         $2(Ca, Ti, LREE, HREE, Th)SiO_5 + 2HPO_4^{2-} + 2HCO_3^{-} \longrightarrow$

558                 $2TiO_2 + 2CaCO_3 + SiO_2 + (LREE, Th)PO_4 + HREEPO_4 \pm ThSiO_4$ (8)

559   The prevalence of phosphates and silicates over fluorocarbonates as principle REE and Th-

560   bearing phases may result from a combination of acidity, mineralogy and the abundance of

561   free phosphate anions. Illite, for example, may have acted as the principle sink for fluorine

562   freed-up from biotite and fluorapatite (Thomas et al., 1977), therefore buffering the activity

563   of F^- in solution.

564

565   The anomalous assemblage with phosphates and fluorocarbonates in K108 may, however,

566   result from minor fluorapatite breakdown and higher pCO_2 relative to K206. Further evidence

567   of locally high CO_2 activity is seen from the presence of ankerite−synchysite-(Ce) veinlets.

568   These veinlets likely formed as a result of contemporaneous titanite breakdown and

569   illitisation-carbonatisation. Following illitisation of major phases and with increasing

570   alkalinity, Ca^{2+}, Fe^{2+}, Mg^{2+} and Mn^{2+} released into solution formed ankerite in pre-existing

571   fractures. As veinlets contain various illite−carbonate overprinting, it is emphasized that fluid

572   flow was episodic (Barker et al., 2006). Crystal growth was most likely initiated by syntaxial

573   blocky quartz (Bons and Montenari, 2005) and ankerite−synchysite-(Ce) followed by illite

574   overprinting and subsequent re-opening. The central Mn-zone-entrained synchysite-(Ce) may

575   have formed by a process of supersaturation−nucleation−depletion (SND) (Barker and Cox,

576   2010; Ortoleva et al., 1987). This particular process can briefly be explained as a fluid

577   reaching a supersaturation point of element X resulting in nucleation and consequent

578   depletion in that element distal from the point of the nucleation.

579

580

581   *5.3.2 REY and Th mobility*

582

583   The behaviour of REY and Th in samples K108 and K206 appears different from sample

584   K177. The difference in mobility may be related to the availability of ligand complexes and

585   the intensity of destructive alteration. A similarity does, however, exists in the enrichment of

586   La (and Ce) in the metasomatic monazite-(Ce) grains (Fig. 10a), which is attributed to

587   processes described above.

588

589   The degree of La enrichment in monazite-(Ce) is, however, smaller relative to synchysite-

590   (Ce). Due to the lack of either Pr_{CN} or Nd_{CN} anomalies, negative La anomalies in monazite-

591   (Ce) could be identified using the methodology of Bau and Dulski (1996). Due to its

592   incompatibility as well as lack of accommodation space in newly precipitated monazite-(Ce)

593   and xenotime-(Y), LREE, particularly La, preferentially remained in solution. The resultant

594   La-rich fluid may therefore account for the later, nearby precipitation of florencite-

595   (La)−florencite-(Ce) solid solutions intergrown with illite veinlets. The prevalence of

596   xenotime-(Y) in K108 and K206 indicates preferential incorporation of middle to HREY;

597   thus a reduction in their mobility relative to K177. As ligands available for complexation,

598   such as HCO_3^- (Bau and Dulski, 1995), were buffered by the presence of divalent cations (Xu

599   et al., 2004) and abundant HPO_4^{2-} remained in solution, middle to HREY are not likely to be

600   mobilised significantly. As such, the middle to HREY element budget was maintained

601   relative to unaltered K102 as seen from the Dy/Lu ratios in Table 1.

602

603

604 With the degree of scatter in Fig. 10d, it is hard to distinguish whether a wholesale loss or

605 gain of Th took place during destabilisation of titanite. However, based on the precipitation of

606 secondary thorite grains within xenotime-(Y), the minor alteration of primary thorite and the

607 maintenance of bulk-rock Th (Table 1) compared to K102, it can be assumed there was

608 minimal mobilisation of Th in K206. Furthermore, the acidity of solution and consequent

609 breakdown of silicates (Reed, 1997) and apatite (Harouiya et al., 2007) would have

610 encouraged Th fixation therefore minimising its mobility. The conversely elevated

611 concentrations of Th (60ppm) in K108 can be attributed to the extensive synchysite-bearing

612 carbonate veinlets, allowing the addition of Th from abundant HCO_3^- or FCO_3^- mobilising

613 ligands.

614

615

616 **6. Conclusions**

617

618 The multifaceted analytical study presented in this paper has proved useful in determining

619 conditions for mineral destabilisation and delineating differential element mobility in

620 geothermal systems:

621   1. Vein–fracture-related alteration significantly modified the original mineralogy with

622   varying intensity. The accessory phases, titanite, allanite-(Ce), apatite and previously

623   unknown uranopolycrase have been altered to, among other minerals, various

624   incompatible element-bearing phases. Alteration products of titanite specifically, are

625   dominated by phosphates or fluorocarbonates and are representative of varying

626   fluid/rock ratios and fluid chemistries.

627   2. Comparative analyses show synchysite-(Ce) depleted in MREE, Y and Th relative to

628   titanite. Thorium concentrations are, however, predominantly maintained in titanite-

629   derived monazite-(Ce) and xenotime-(Y), whereas middle to heavy REE are

630   preferentially incorporated into xenotime-(Y). The REE, Y and Th are comparatively

631   immobile in samples containing hydrothermal monazite and xenotime due to the

632   abundance of free HPO_4^{2-} in solution. However, depleted MREE, Y and Th

633   concentrations in synchysite-(Ce) indicate not only a lack of accommodation space

634   but a significantly increased mobility of those elements in hydrothermal solutions

635   dominated by (bi)-ligands such as FCO_3^- and/or HCO_3^-.

636 Although not fully constrained for the Soultz monzogranite, determining the full extent of Th

637 mobilisation is of significant importance when trying to understand HHP element enrichment

638 in granitic hydrothermal systems.

639

640

650

651 **References**

652 Alexandrov, P., Royer, J.-J., Deloule, E., 2001. 331 ± 9Ma emplacement age of the Soultz

653   monzogranite (Rhine Graben basement) by U/Pb ion-probe zircon dating of samples from

654   5km depth. CR. Acad. Sci. 332 (12), 747-754.

655   Aquilina, L., Pauwels, H., Genter, A., Fouillac, C., 1997. Water-rock interaction processes in the

656   Triassic sandstone and the granitic basement of the Rhine Graben: Geochemical

657   investigations of a geothermal reservoir. Geochim. Cosmochim. Acta. 61 (20), 4281-4295.

658   Armstrong, J.T., 1995. CITZAF: A package of correction programs for the quantitative electron

659   microbeam analysis of thick polished materials, thin films, and particle. Microbeam Anal. 4,

660   177-200.

661   .Bancroft, G.M., Metson, J.B., Kresovic, R.A., Nesbitt, H.W., 1987. Leaching studies of natural and

662   synthetic titanties using secondary ion mass spectrometry. Geochim. Cosmochim. Acta. 51,

663   911-918.

664   Barclay, S.A., Worden, R.H., 2000. Geochemical modelling of diagenetic reactions in a sub-arkosic

665   sandstone. Clay Miner. 35, 57-67.

666   Barker, S.L.L., Cox, S.F., 2010. Oscillatory zoning and trace element incorporation in hydrothermal

667   minerals: insights fom calcite growth experiments. Geofluids. 11 (1), 48-56.

668   Barker, S.L.L., Cox, S.F., Eggins, S.M., Gagan, M.K., 2006. Microchemical evidence for episodic

669   growth of individual growth of antitaxial veins during fracture-controlled fluid flow. Earth

670   Planet. Sci. Lett. 250, 331-344.

671   Bau, M., 1991. Rare-earth element mobility during hydrothermal and metamorphic fluid-rock

672   interaction and the significance of the oxidation state of europium. Chem. Geol. 93, 219-230.

673   Bau, M., Dulski, P., 1995. Comparative study of yttrium and rare-earth element behaviours in

674   fluorine-rich hydrothermal fluids. Contrib. Mineral. Petr. 119, 213-223.

675   Bau, M., Möller, P., 1991. REE systematics as source of information on minerogenesis. In: Pagel, M.,

676   Leroy, J.L. (Eds.), Source, Transport and Deposition of Metals. A. A. Balkema, Rotterdam.

677   Bea, F., 1996. Residence of REE, Y, Th and U in Granites and Crustal Protoliths; Implications for the

678   Chemistry of Crustal Melts. J. Petrol. 37 (3), 521-552.

679   Bohlen, S.R., Essene, E.J., 1978. The significance of metamorphic fluorite in the Adirondacks.

680   Geochim. Cosmochim. Acta. 42, 1669-1678.

681   Bons, P.D., Montenari, M., 2005. The formation of antiaxial calcite veins with well-developed fibres,

682   Oppaminda Creek, South Australia. J. Struct. Geol. 27, 231-248.

683   Bonyadi, Z., Davidson, G.J., Mehrabi, B., Meffre, S., Ghazban, F., 2011. Significance of apatite REE

684   depletion and monazite inclusions in the brecciated Se-Chahun iron oxide-apatite deposit,

685   Bafq district, Iran: Insights from paragenesis and geochemistry. Chem. Geol. 281, 253-269.

686   Coppin, F., Berger, G., Bauer, A., Castet, S., Loubet, M., 2002. Sorption of lanthanides on smectite

687   and kaolinite. Chem. Geol. 182, 57-68.

688   Corlett, M.I., McIlreath, I.A., 1974. An authigenic Quartz-Calcite-Rutile Assemblage in Ordovician

689   Limestones. Can. Mineral. 12, 411-416.

690   Cuney, M., Friedrich, M., 1987. Physicochemical and crystal-chemical controls on accessory mienral

691   paragenesis in granitoids: implications for uranium metallogenesis. B. Mineral. 110 (5), 235-

692   247.

693   Dubois, M. et al., 1996. Temperature of palaeo- to modern self-sealing within a continental rift basin:

694   The fluid inclusion data (Soultz-sous-Forêts, Rhine graben, France). Eur. J. Mineral. 8, 1065-

695   1080.

696   Eggins, S.M.W., J. D. et al., 1997. A simple method for the precise determination of $\geq$ 40 trace

697   elements in geological samples by ICPMS using enriched isotope internal standardisation.

698   Chem. Geol. 134 (4), 311-326.

699   Förster, H.-J., 2000. Cerite-(Ce) and Thorian Synchysite-(Ce) from the Niederbobritzsch Granite,

700   Erzegebirge, Germany: Implications for the Differential Mobility of the LREE and Th during

701   Alteration. Can. Mineral. 38, 67-79.

702   Förster, H.-J., 2001. Synchysite-(Y)-synchysite-(Ce) solid solutions from Markersbach, Erzgebirge,

703   Germnay: REE and Th mobility during high-T alteration of highly fractionated aluminous A-

704   type granites. Mineral. Petrol. 72, 259-280.

705   Förster, H.-J., Tischendorf, G., Trumbull, R.B., Gottesmann, B., 1999. Late-collisional granites in the

706   Variscan Erzgebirge, Germany. J. Petrol. 40 (11), 1613-1645.

707   Fouillac, A.M., Genter, A., 1992. An O, D, C isotopic study of water/rock interactions in the Soultz-

708   sous-Forêts granite. In: Bresee, J.C. (Ed.), Geothermal Energy in Europe: The Soultz hot dry

709   rock project. Gordon and Breach Science Publishers, Montreux, pp. 105-118.

710 Genter, A., Traineau, H., 1991. Geological survey of the HDR borehole EPS-1, Soultz-sous-Forêts,

711   Alsace, France. R 32433.

712 Giére, R., 1990. Hydrothermal mobility of Ti, Zi and REE: examples from the Bergell and Adamello

713   contact aureoles (Italy). Terra Nova. 2, 60-67.

714 Gradstein, F.M., Ogg, J., 1997. A Phanerozoic timescale. Episodes. 19, 3-5.

715 Gromet, L.P., Silver, L.T., 1983. Rare earth element distributions amoung minerals in a granidiorite

716   and their petrogenetic implications. Geochim. Cosmochim. Acta. 47, 925-939.

717 Harlov, D.E., Förster, H.-J., 2003. Fluid-induced nucleation of (Y+REE)-phosphate minerals within

718   apatite: Nature and experiment. Part II. Fluoroapatite. Am. Mineral. 88, 1209-1229.

719 Harlov, D.E., Förster, H.-J., Nijland, T.G., 2002. Fluid-induced nucleation of (Y+REE)-phosphate

720   minerals within apatite: Nature and experiment. Part I. Chlorapatite. Am. Mineral. 87, 245-

721   261.

722 Harlov, D.E., Wirth, R., Förster, H.-J., 2005. An experimental study of dissolution–reprecipitation in

723   fluorapatite: fluid infiltration and the formation of monazite. Contrib. Mineral. Petr. 150, 268-

724   286.

725 Harouiya, N., Chaïrat, C., Köhler, S.J., Gout, R., Oelkers, E.H., 2007. The dissolution kinetics and

726   apparent solubility of natural apatite in closed reactors ar temperatures from 5 to 50°C and pH

727   from 1 to 6. Chem. Geol. 244, 554-568.

728 Hunt, J.A., Kerrick, D.M., 1977. The stability of sphene: experimental redetermination and geologic

729   implications. Geochim. Cosmochim. Acta. 41, 279-288.

730 Kominou, A., Yardley, B.W.D., 1997. Fluid-rock interactions in the Rhine Graben: A thermodynamic

731   model of the hydrothermal alteration observed in deep drilling. Geochim. Cosmochim. Acta.

732   61 (3), 515-531.

733 Ledésert, B. et al., 2010. Fractures, hydrothermal alterations and permeability in the Soultz Enhanced

734   Geothermal System. CR. Geo. 342, 607-615.

735 Lowenstern, J.B., 2001. Carbon dioxide in magmas and implications for hydorthermal systems.

736   Miner. Deposita. 36, 490-502.

737   Ortoleva, P., Merino, E., Moore, C., Chadam, J., 1987. Geochemical self-organisation 1: Reaction-

738   transport feedbacks and modeling approach. Am. J. Sci. 287, 979-1007

739

740   Pan, Y., Fleet, M., MacRae, N., 1993. Late alteration in titanite ($CaTiSiO_5$): Redistribution and

741   remobilisation of rare earth elements and implications for U/Pb and Th/Pb geochronology and

742   nuclear waste disposal. Geochim. Cosmochim. Acta. 57, 355-367.

743   Pan, Y., Fleet, M.E., 2002. Composition of the apatite-group minerals: substitution and controlling

744   factors. In: Kohn, M.J., Rakovan, J., Hughes, J.M. (Eds.), Phosphates: geochemical,

745   geobiological and materials importance. Reviews in Mineralogy, Mineralogical Society of

746   America, Washington D.C., pp. 13-49.

747   Pauwels, H., Fouillac, C., Fouillac, A.M., 1993. Chemistry and isotopes of deep geothermal saline

748   fluids in the Upper Rhine Graben: Origin of compounds and water-rock interactions.

749   Geochim. Cosmochim. Acta. 57, 2737-2749.

750   Reed, M.H., 1997. Hydrothermal alteration and its relationship to ore fluid composition. In: Barnes,

751   H.L. (Ed.), Geochemistry of Hydrothermal Ore Deposits. Wiley, New York, pp. 303-366.

752   Salvi, S., William-Jones, A.E., 1990. The role of hydrothermal processes in the granite-hosted Zr, Y,

753   REE deposit at Strange Lake, Quebec / Labrador: Evidence from fluid inclusions. Geochim.

754   Cosmochim. Acta. 54 (2403-2418).

755   Salvi, S., William-Jones, A.E., 1996. The role of hydrothermal processes in concentrating high-field

756   strength elements in the Strange Lake peralkaline complex, northeastern Canada. Geochim.

757   Cosmochim. Acta. 11, 1917-1932.

758   Sanematsu, K., Kon, Y., Imai, A., Watanabe, K., Watanabe, Y., 2011. Geochemical and mineralogical

759   characteristics of ion-adsorption type REE mineralization in Phuket, Thailand. Miner.

760   Deposita, 1-15.

761   Simon, K., 1990. Hydrothermal alteration of Variscan granites, southern Schwarzwald, Federal

762   Republic Germany. Contrib. Mineral. Petr. 105, 177-196.

763 Stussi, J.-M., Cheilletz, A., Royer, J.-J., Chèvremont, P., Féraud, G., 2002. The hidden monzogranite
764   of Soultz-sous-Forêts (Rhine Graben, France). Mineralogy, petrology and genesis. Geol.
765   France (1), 45-64.

766 Thomas, J., Jr., Glass, H.D., White, W.A., Trandel, R.M., 1977. Fluoride content of clay minerals and
767   argillaceous earth materials. Clays Clay Miner. 25, 278-284.

768 Torab, F.M., Lehmann, B., 2007. Magnetite-apatite deposits of the Bafq district, Central Iran: apatite
769   geochemistry and monazite geochronology. Mineral. Mag. 71 (3), 347-363.

770 Troitzsch, U., Ellis, D.J., 2002. Thermodynamic properties and stability of AlF-bearing titanite
771       $CaTiOSiO_4$-Ca-$AlFSiO_4$. Contrib. Mineral. Petr. 142, 543-563.

772 Uysal, I.T. et al., 2011. Trace element composition of near-surface silica deposits - A powerful tool
773   for detecting hydrothermal mineral and energy resources. Chem. Geol. 280, 154-169.

774 Wang, L., Ni, Y., Hughes, J.M., Bayliss, P., Drexler, J.W., 1994. The atomic arrangement of
775   synchysite-(Ce), $CeCaF(CO_3)_2$ Can. Mineral. 32 (865-871).

776 Watt, G., Harley, S., 1993. Accessory phase controls on the geochemistry of crustal melts and restites
777   produced during water-undersaturated partial melting. Contrib. Mineral. Petr. 114, 550-566.

778 William-Jones, A.E., 1981. Thermal Metamorphism of Siliceous Limestone in the Aureole of Mount
779   Royal, Quebec. Am. J. Sci. 281, 673-696.

780 Wolf, M., London, D., 1994. Apatite dissolution into peraluminous haplogranitic melts: An
781   experimental study of solubilities and mechanisms. Geochim. Cosmochim. Acta. 58 (19),
782   4127-4145.

783 Wood, S.A., 1990a. The aqueous geochemistry of the rare-earth elements and yttrium, 1. Review of
784   available low-temperature data for inorganic REE speciation of natural waters. Chem. Geol.
785   82, 159-186.

786 Wood, S.A., 1990b. The aqueous geochemistry of the rare-earth elements and yttrium: 2. Theoretical
787   predictions of speciation in hydrothermal solutions to 350°C at saturation water vapour
788   pressure. Chem. Geol. 88, 99-125.

789 Xie, L., Wang, R.-C., Chen, J., Zhu, J.-C., 2010. Mineralogical evidence for magmatic and

790   hydrothermal process in the Qitianling oxidised tin-bearing granite (Hunan, south China):

791   EMP and (MC)-LA-ICPMS investigations of three types of titanite. Chem. Geol. 276, 53-68.

792 Xu, T., Apps, J.A., Pruess, K., 2004. Numerical simulation of CO_2 disposal by mineral trapping in

793   deep aquifers. Appl. Geochem. 19, 917-936.

794 Zen, E.-A., 1986. Aluminium Enrichment in Silicate Melts by Fractional Crystallisation: Some

795   Mineralogic and Petrogrpahic Constraints. J. Petrol. 27, 1095-1117.

796

798 **Figure captions**

799 Figure 1 (a+b)

800 BSE photomicrographs from K102 of (a) patchy-zoned, euhedral primary allanite with darker

801 localised domains of epidotisation (arrow), (b) oscillatory-zoned euhedral titanite with partial

802 alteration to brighter allanite (arrow).

803

804 Figure 2 (a)

805 BSE photomicrograph from K177 of destabilised titanite forming anatase (Ant) + calcite

806 (Cal) + quartz (Qz) + synchysite-(Ce) (Syn).

807

808 Figure 3 (a+b)

809 BSE photomicrographs from K177 of (a) intensively oscillatory-zoned fluorapatite showing

810 (b) local REE-depletion (Dep) domains (dark) where small monazite (Mnz) grains formed as

811 result of dissolution-reprecipitation processes.

812

813 Figure 4 (a+b)

814 BSE photomicrographs from K177 of (a) allanite altered to calcite (Cal) + illite (Ill) + anatase

815 (Ant) + quartz (Qz), with fracture-grown synchysite + bastnaesite + thorite intergrowths

816 proximal to hematite-magnetite grains (Hem-Mag); (b) high-contrast image of synchysite

817 (Syn), bastnaesite (Bas) and thorite (Thr) seen in (a).

818

819 <u>Figure 5</u>

BSE photomicrograph from K177 of uranopolycrase altered to Nb-rich anatase (Ant) +

rutherfordine (Rtd) + quartz (Qz) + illite (Ill).

820

821 <u>Figure 6</u>

822 BSE photomicrograph from K206 of an anhedral fluorapatite broken down by CO_2 + KCl-

823 rich solution, as seen by the invasive illite veinlets (arrow) (K206).

824

825 <u>Figure 7</u>

826 BSE photomicrographs from K206 of (a) destabilised titanite forming anatase (Ant) + calcite

827 (Cal) + quartz (Qz) + monazite (Mnz) + xenotime (Xtm) + thorite (Thr); (b) high contrast

828 image of monazite, xenotime and xenotime enclosed thorite.

829

830 <u>Figure 8</u>

831 Chondrite-normalised REY distribution patterns for (a) whole-rock analyses of K102 (circle),

832 K108 (square), K177 (diamond) and K206 (triangle); (b) allanite (square) and titanite

833 (triangle); (c) primary thorite (square – K108 and circle – K206); (d) synchysite-(Ce) (square

834 and triangle) formed in response to titanite dissolution and bastnaesite-(Ce) (circle) produced

835 during destabilisation of allanite-(Ce); (e) monazite-(Ce) formed in response to titanite

836 dissolution (triangle), monazite-(Ce) forming inclusions in fluorapatite (circle), and

837 monazite-(Ce) produced during destabilisation of allanite-(Ce) (square); (f) xenotime-(Y)

838 (K108 – square and K206 – triangle).

839

840   Figure 9

841   RAMAN spectra for (a) synchysite-(Ce) with nano-scale anatase inclusions; (b) an anatase

842   grain; and (c) synchysite-(Ce) with little or no anatase. All analyses are from sample K177.

843

844   Figure 10
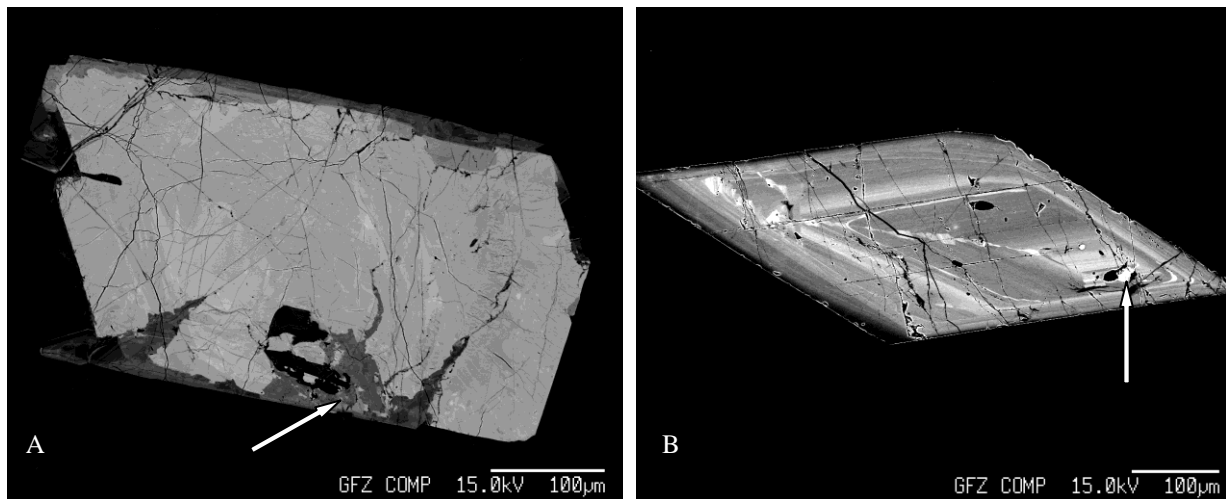
845   Plots of (a) La % of REE + Y versus Σ REE + Y, (b) Y % of REE + Y versus Σ REE + Y, (c)

846   Dy % of REE + Y versus Σ REE + Y and (d) Th % of REY + Th versus ΣREY + Th.

847   Triangle = titanite, square = synchysite, diamond = monazite and cross = xenotime.

848

849   **Figure 1**

850

36

851
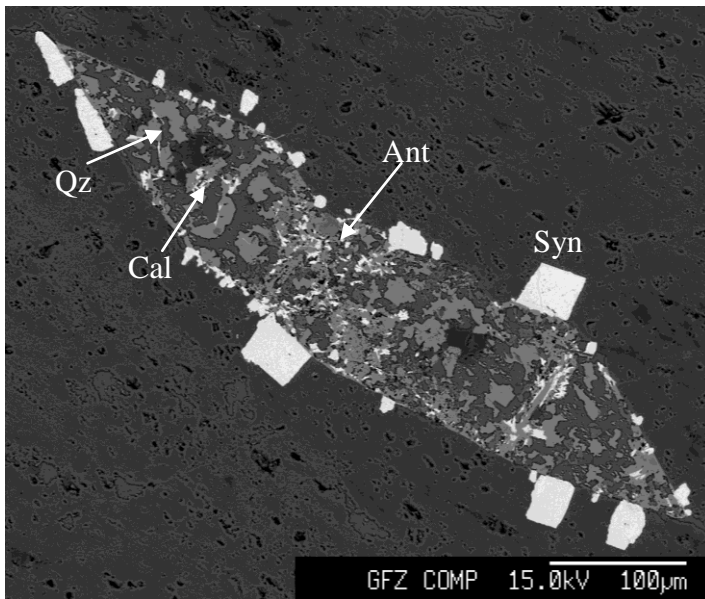
Middleton et al.: Figure 2

853

854
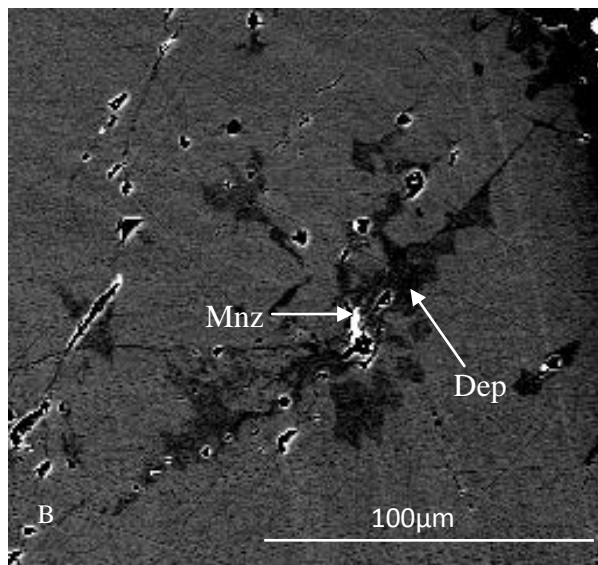
Middleton et al. Figure 3

856

857

Middleton et al. Figure 4

859

Middleton et al. Figure 5

861

862

863 **Middleton et al. Figure 6**
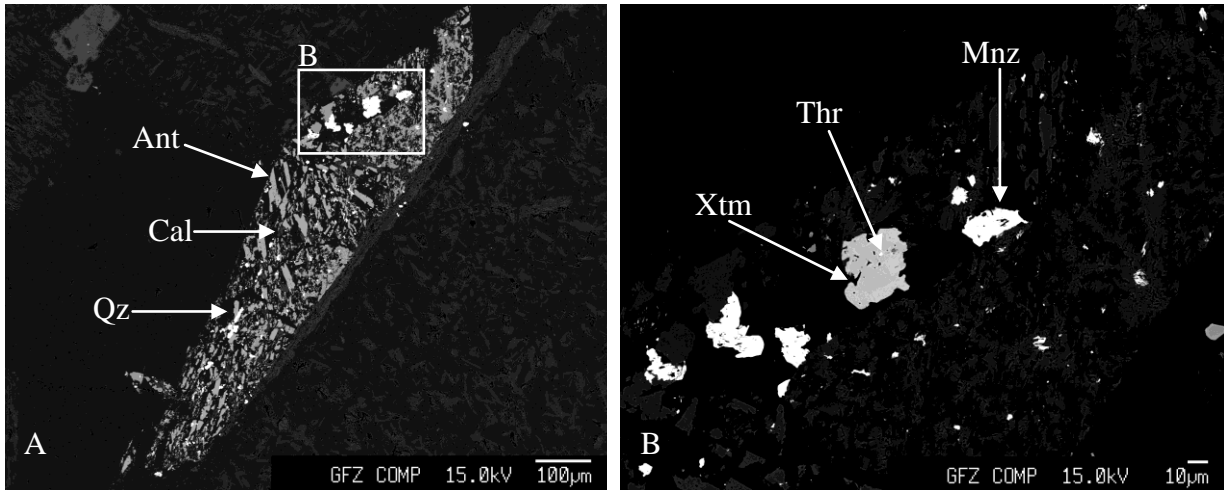
864

865 **Middleton et al. Figure 7**

866

867

868
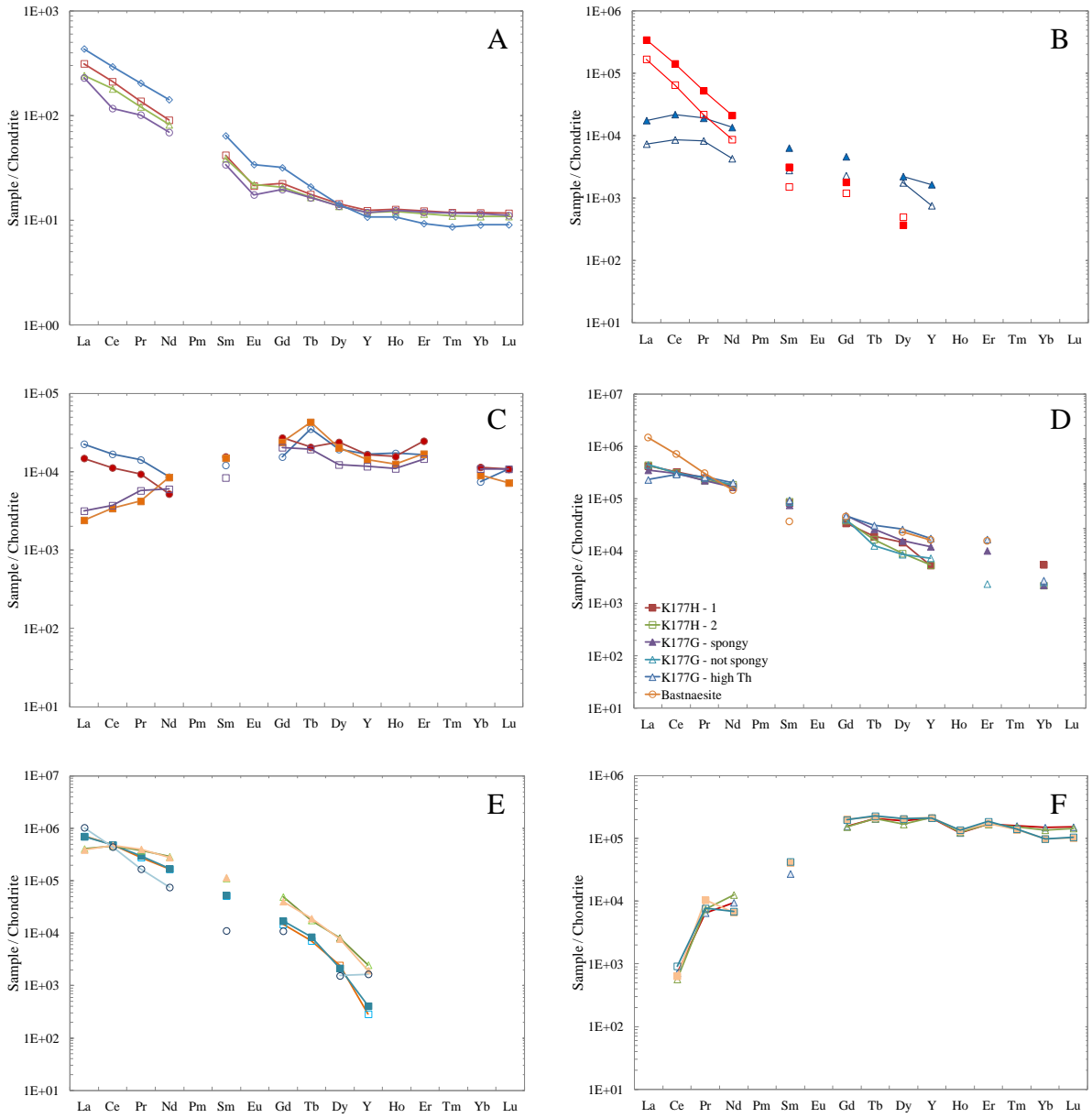
869

870 **Middleton et al. Figure 8**

871

872

873
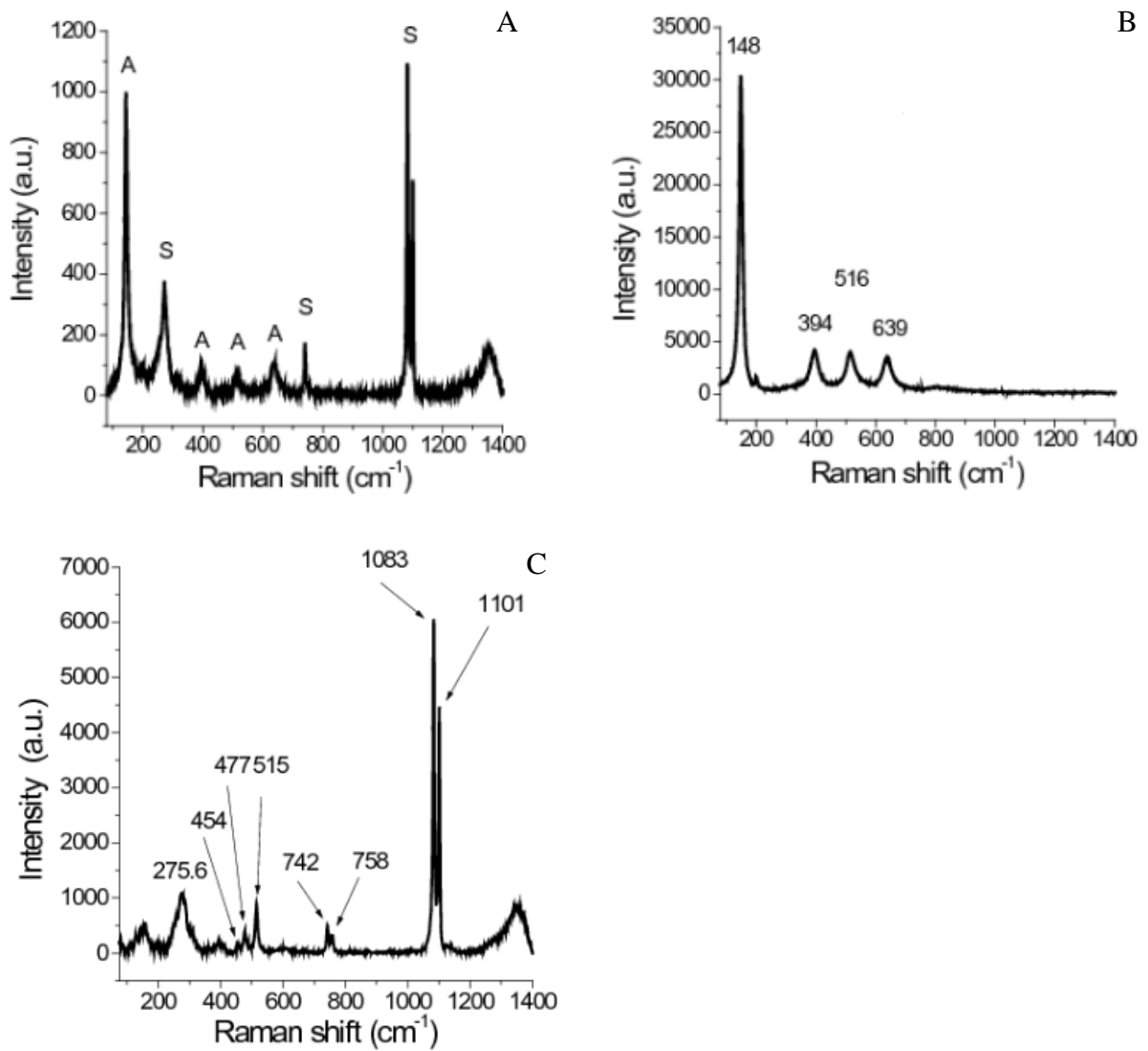
874

875 **Middleton et al. Figure 9**

876

877
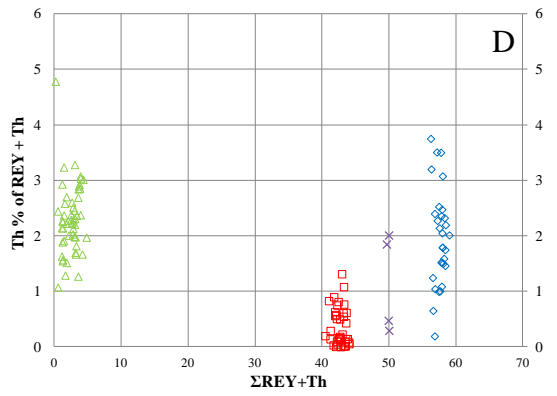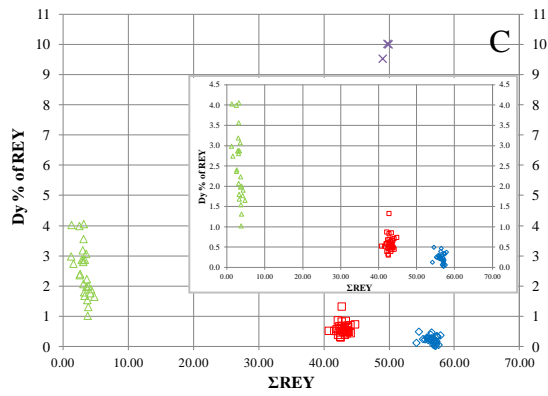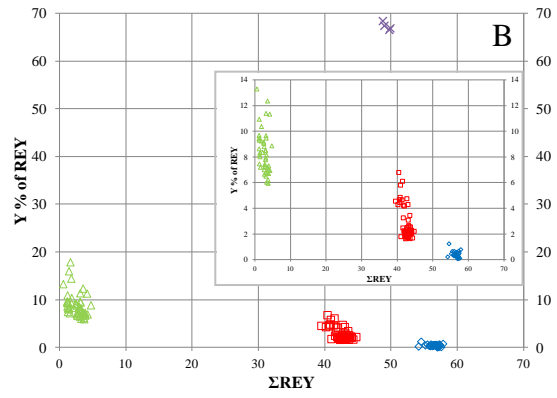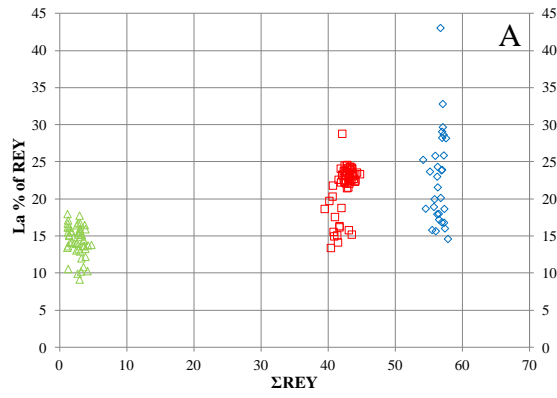
878

879

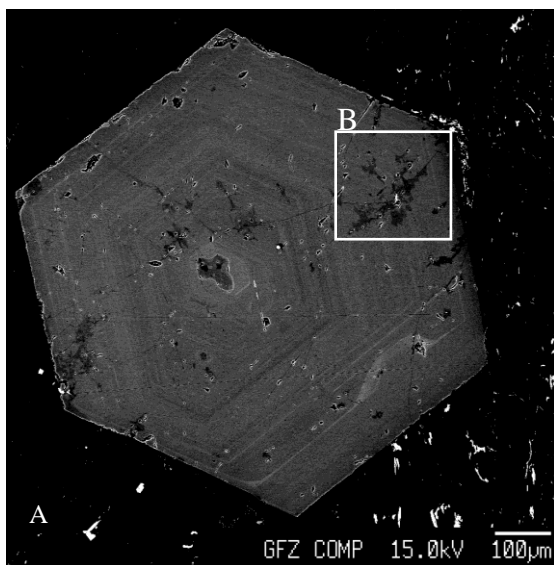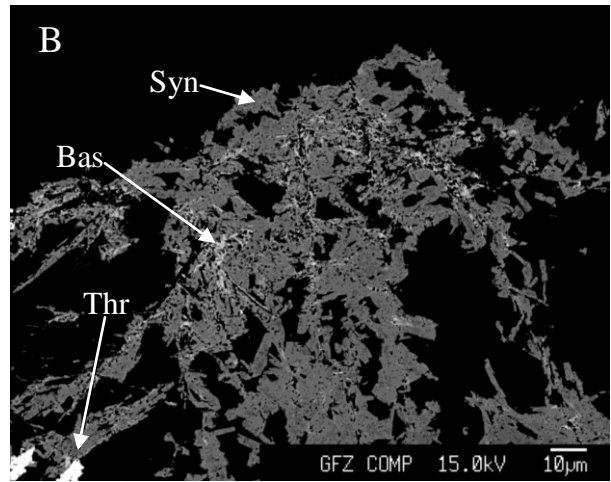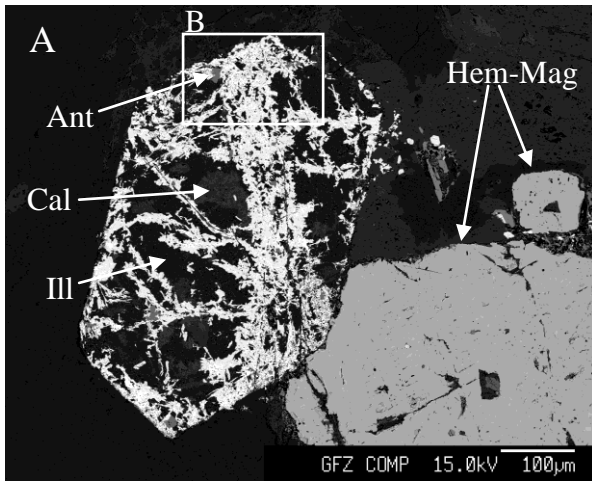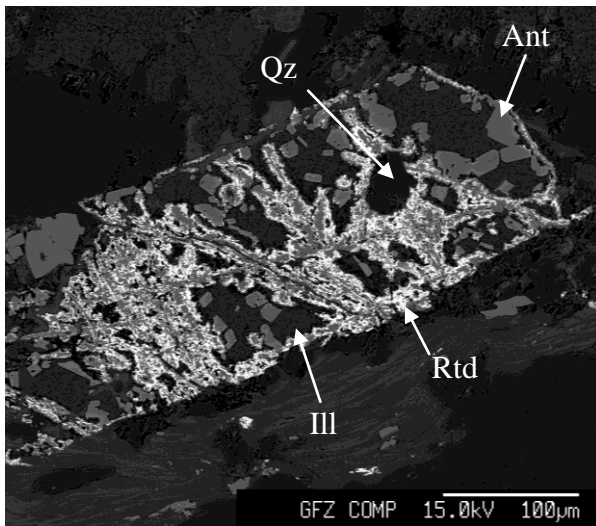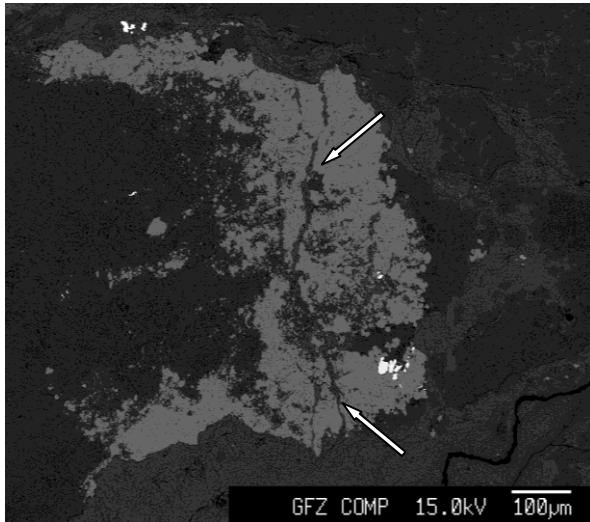880 **Middleton et al. Figure 10**

881

882

Table 1. Major- and selected trace-element concentrations of whole-rock samples

Sample	K102	K108	K177	K206
SiO_2 (wt%)	69.1	68.6	64.4	63.0
TiO_2	0.54	0.57	0.56	0.57
Al_2O_3	14.1	14.8	15.4	15.5
Fe_2O_3[a]	2.98	2.18	6.28	2.19
MnO	0.08	0.12	0.04	0.08
MgO	1.31	0.81	1.50	0.59
CaO	1.72	1.76	0.91	3.74
Na_2O	3.83	1.63	2.36	2.85
K_2O	5.72	6.55	5.62	6.05
P_2O_5	0.24	0.33	0.29	0.26
F	0.09	0.12	0.10	0.09
LOI	0.76	3.28	2.48	3.72
Total	100	100	99.9	98.6
La (ppm)	52.2	71.2	98.8	54.9
Ce	71.8	129	180	111
Pr	9.65	13.1	19.5	11.6
Nd	32.3	42.3	66.5	38.3
Sm	5.21	6.42	9.84	5.93
Eu	1.02	1.24	1.98	1.27
Gd	4.05	4.60	6.55	4.23
Tb	0.61	0.66	0.78	0.62
Dy	3.48	3.66	3.62	3.47
Y	18.6	19.3	16.8	18.6
Ho	0.70	0.72	0.61	0.68
Er	1.98	2.03	1.54	1.91
Tm	0.30	0.30	0.22	0.28
Yb	1.96	2.01	1.53	1.85
Lu	0.28	0.30	0.23	0.28
ΣREY	204	297	408	254
Th	23.7	59.6	67.0	24.2
U	2.11	13.4	20.9	6.96
La/Lu	185	240	429	198
Dy/Lu	12.3	12.3	15.7	12.5

885

Table 2 Composition (in wt%) of titanite and allanite-(Ce) from sample K102

Sample	Det. limit (ppm)	Ttn 1 Aver. (n=23)	*Min – Max*	Ttn 2. Aver.(n=30)	*Min – Max*	Ep Aver. (n=8)	*Min – Max*	Aln Aver. (n=6)	*Min – Max*
Nb$_2$O$_5$	52	0.75	*(0.14 – 2.79)*	0.49	*(0.28 – 0.99)*				
Ta$_2$O$_5$	245	b.d.l.	*(0.00 – 0.70)*	0.05	*(0.00 – 0.20)*				
SnO$_2$	48	0.05	*(0.03 – 0.12)*	0.04	*(0.02 – 0.07)*				
SiO$_2$	75	30.6	*(29.86 – 30.93)*	30.1	*(29.61 – 30.48)*	35.3	*(33.79 – 36.41)*	32.0	*(31.31 – 32.68)*
TiO$_2$	180	35.4	*(31.37 – 37.22)*	35.5	*(34.50 – 36.31)*	0.20	*(0.04 – 0.67)*	1.32	*(0.48 – 1.55)*
ZrO$_2$	88	0.05	*(0.01 – 0.24)*	0.09	*(0.04 – 0.19)*				
ThO$_2$	39	0.04	*(0.01 – 0.07)*	0.09	*(0.05 – 0.15)*	0.66	*(0.18 – 1.49)*	1.41	*(1.33 – 1.60)*
UO$_2$	106	0.03	*(0.00 – 0.06)*	0.01	*(0.00 – 0.04)*	0.03	*(0.01 – 0.05)*	0.03	*(0.01 – 0.06)*
Al$_2$O$_3$	42	1.43	*(1.07 – 1.82)*	1.32	*(1.15 – 1.47)*	19.3	*(16.39 – 20.87)*	12.6	*(11.11 – 15.46)*
Y$_2$O$_3$	64	0.18	*(0.00 – 0.37)*	0.33	*(0.22 – 0.59)*	0.00	*(0.00 – 0.00)*	0.00	*(0.00 – 0.00)*
La$_2$O$_3$	198	0.22	*(0.05 – 0.39)*	0.48	*(0.32 – 0.69)*	4.66	*(3.21 – 7.62)*	9.63	*(8.41 – 10.65)*
Ce$_2$O$_3$	184	0.68	*(0.12 – 1.17)*	1.55	*(01.07 – 2.04)*	4.63	*(3.27 – 6.88)*	10.1	*(7.98 – 11.21)*
Pr$_2$O$_3$	271	0.07	*(0.00 – 0.18)*	0.20	*(0.12 – 0.33)*	0.23	*(0.17 – 0.36)*	0.54	*(0.33 – 0.66)*
Nd$_2$O$_3$	246	0.26	*(0.01 – 0.49)*	0.72	*(0.53 – 1.15)*	0.46	*(0.39 – 0.56)*	1.07	*(0.68 – 1.31)*
Sm$_2$O$_3$	253	0.05	*(0.00 – 0.14)*	0.11	*(0.05 – 0.21)*	b.d.l.	*(0.00 – 0.04)*	0.02	*(0.00 – 0.11)*
Gd$_2$O$_3$	267	0.04	*(0.00 – 0.11)*	0.10	*(0.02 – 0.22)*	0.02	*(0.00 – 0.05)*	0.02	*(0.00 – 0.07)*
Dy$_2$O$_3$	293	0.03	*(0.00 – 0.10)*	0.06	*(0.00 – 0.13)*	0.02	*(0.00 – 0.07)*	0.00	*(0.00 – 0.01)*
FeO	112	1.90	*(01.10 – 2.82)*	1.83	*(01.56 – 2.10)*	13.2	*(12.52 – 14.09)*	12.9	*(11.33 – 14.48)*
CaO	30	27.5	*(26.83 – 28.30)*	26.0	*(25.75 – 27.01)*	17.5	*(14.31 – 19.44)*	11.8	*(11.29 – 13.05)*
MgO	48	0.03	*(0.01 – 0.06)*	0.03	*(0.01 – 0.05)*	0.25	*(0.11 – 0.67)*	1.01	*(0.58 – 1.66)*
MnO	77	0.24	*(0.20 – 0.35)*	0.21	*(0.17 – 0.24)*	0.75	*(0.62 – 0.87)*	1.21	*(0.70 – 1.65)*
Total		99.5		99.9		97.1		95.8	
ΣREY$_2$O$_3$		1.54	*(0.18 – 2.96)*	3.65	*(2.33 – 5.36)*	10.0	*(7.04 – 15.57)*	21.3	*(17.41 – 24.03)*

886 Aver. = average, Ttn = titanite, Ep = REE-rich epidote, Aln = allanite-(Ce), blank = not analysed, b.d.l. = below detection limit.

Table 3. Composition (in wt%) of thorite from samples K108 and K206

Sample	Det. limit (ppm)	K108 Aver. (n= 14)	Min – Max	K206 Aver. (n=2)	Min – Max
P$_2$O$_5$	100	3.62	*(2.96 – 4.13)*	2.53	*(2.39 – 2.66)*
SiO$_2$	115	16.3	*(15.41 – 16.89)*	18.1	*(17.67 – 18.44)*
TiO$_2$	333	0.05	*(0.00 – 0.09)*	0.03	*(0.01 – 0.05)*
ZrO$_2$	203	1.19	*(0.40 – 2.59)*		
ThO$_2$	77	62.9	*(58.96 – 65.41)*	60.5	*(59.92 – 61.15)*
UO$_2$	203	4.57	*(3.06 – 6.37)*	6.23	*(5.97 – 6.49)*
Al$_2$O$_3$	70	0.13	*(0.06 – 0.25)*	0.47	*(0.28 – 0.65)*
Y$_2$O$_3$	142	2.82	*(2.32 – 3.38)*	3.30	*(3.28 – 3.32)*
La$_2$O$_3$	511	0.10	*(0.05 – 0.17)*	0.52	*(0.41 – 0.62)*
Ce$_2$O3	446	0.22	*(0.14 – 0.29)*	0.99	*(0.80 – 1.19)*
Pr$_2$O$_3$	694	b.d.l.	*(0.01 – 0.07)*	0.12	*(0.10 – 0.15)*
Nd$_2$O$_3$	630	0.37	*(0.23 – 0.48)*	0.36	*(0.28 – 0.45)*
Sm$_2$O$_3$	539	0.24	*(0.14 – 0.31)*	0.24	*(0.21 – 0.27)*
Gd$_2$O$_3$	714	0.55	*(0.39 – 0.66)*	0.48	*(0.35 – 0.62)*
Tb$_2$O$_3$	607	0.13	*(0.06 – 0.20)*	0.12	*(0.09 – 0.15)*
Dy$_2$O$_3$	633	0.55	*(0.34 – 0.71)*	0.60	*(0.54 – 0.67)*
Ho$_2$O$_3$	650	0.08	*(0.06 – 0.10)*	0.11	*(0.10 – 0.11)*
Er$_2$O$_3$	750	0.28	*(0.20 – 0.49)*	0.38	*(0.30 – 0.45)*
Yb$_2$O$_3$	375	0.17	*(0.11 – 0.23)*	0.18	*(0.14 – 0.21)*
Lu$_2$O$_3$	398	b.d.l.	*(0.00 – 0.04)*	0.03	*(0.03 – 0.03)*
CaO	53	1.12	*(0.80 – 1.45)*	0.44	*(0.44 – 0.45)*
FeO	224	0.18	*(0.07 – 0.38)*	0.15	*(0.13 – 0.17)*
PbO	118	0.06	*(0.02 – 0.15)*	0.18	*(0.15 – 0.20)*
Total		95.6		96.0	
ΣREY$_2$O$_3$		5.59	*(4.65 – 6.91)*	7.42	*(7.29 – 7.56)*

887   Aver. = average, blank = not analysed, b.d.l. = below detection limit.

888

Table 4. Composition (in wt%) of bastnaesite-(Ce) and synchysite-(Ce) from sample K177

Sample	Det. limit (ppm)	Bas	Syn 1 Aver.(n=20)	*Min – Max*	Syn 2 Aver.(n=30)	*Min – Max*
P_2O_5	99	0.07	0.01	(0.00 – 0.05)	0.04	(0.00 – 0.50)
SiO_2	83	0.41	0.67	(0.18 – 1.43)	0.72	(0.14 – 1.33)
TiO_2	478	0.00	0.40	(0.02 – 1.26)	0.35	(0.00 – 0.92)
ZrO_2	195	0.00	0.00	(0.00 – 0.01)	0.00	(0.00 – 0.02)
ThO_2	127	1.29	0.24	(0.03 – 0.61)	0.11	(0.00 – 0.54)
UO_2	359	0.00	b.d.l.	(0.00 – 0.12)	b.d.l.	(0.00 – 0.06)
Al_2O_3	72	0.33	0.21	(0.02 – 0.46)	0.27	(0.10 – 0.66)
Y_2O_3	255	1.12	1.35	(0.96 – 2.58)	1.18	(0.88 – 2.23)
La_2O_3	953	29.6	11.6	(10.42 – 12.38)	11.7	(7.77 – 14.22)
Ce_2O_3	862	32.6	22.6	(21.26 – 23.46)	22.9	(20.97 – 25.49)
Pr_2O_3	1306	1.80	2.44	(2.09 – 2.70)	2.55	(1.91 – 3.12)
Nd_2O_3	1364	3.85	9.19	(8.43 – 9.75)	9.50	(5.63 – 11.94)
Sm_2O_3	1069	0.25	1.39	(1.20 – 1.65)	1.42	(0.35 – 1.89)
Gd_2O_3	1070	0.43	1.02	(0.71 – 1.34)	0.95	(0.15 – 1.36)
Tb_2O_3	1198		b.d.l.	(0.04 – 0.15)	b.d.l.	(0.00 – 0.20)
Dy_2O_3	1149	0.24	0.30	(0.16 – 0.67)	0.28	(0.00 – 0.59)
Er_2O_3	1422	b.d.l.	b.d.l.	(0.00 – 0.17)	b.d.l.	(0.00 – 0.08)
Yb_2O_3	695	b.d.l.	b.d.l.	(0.00 – 0.15)	b.d.l.	(0.00 – 0.16)
CaO	75	1.51	16.79	(16.55 – 17.17)	16.8	(16.53 – 17.90)
FeO	360	0.24	0.10	(0.00 – 0.36)	0.08	(0.00 – 0.50)
F	393	7.93	5.50	(5.16 – 5.76)	5.40	(4.57 – 5.75)
$F=O_2$		3.34	2.31	(2.17 – 2.42)	2.27	(1.92 – 2.42)
Total		78.4	71.6		72.1	
ΣREY_2O_3		69.9	49.9	(47.78 – 51.11)	50.6	(49.07 – 52.41)

Aver. = average, Bas = bastnaesite-(Ce), Syn = synchysite-(Ce), blank = not analysed, b.d.l. = below detection limit.

Table 5. Composition (in wt%) of monazite (Mnz) derived from altered titanite (Ttn) and apatite (Ap) in samples K108 and K206.

Sample		K108		K206				
	Det. limit (ppm)	Mon (Ttn) Aver. (n=16)	*Min – Max*	Mon (anomalous)	Mon (Ttn) Aver. (n=7)	*Min – Max*	Mon (Ap) (n=7)	*Min – Max*
P_2O_5	91	29.6	*(29.01 – 30.05)*	30.2	29.8	*(29.55 – 30.03)*	30.4	*(30.24 – 30.58)*
SiO_2	92	0.50	*(0.13 – 0.91)*	0.20	0.66	*(0.46 – 0.77)*	0.24	*(0.23 – 0.28)*
TiO_2	277	0.35	*(0.00 – 0.67)*	0.11	0.81	*(0.38 – 1.04)*	0.02	*(0.01 – 0.05)*
ThO_2	64	1.42	*(0.42 – 2.40)*	0.12	1.33	*(0.65 – 2.05)*	1.07	*(0.66 – 1.46)*
UO_2	176	0.00	*(0.00 – 0.04)*	0.00	0.00		0.01	*(0.00 – 0.02)*
Al_2O_3	58	0.24	*(0.04 – 0.57)*	0.50	0.26	*(0.04 – 0.53)*	0.34	*(0.28 – 0.44)*
Y_2O_3	129	0.33	*(0.15 – 0.58)*	0.33	0.42	*(0.19 – 0.86)*	0.09	*(0.06 – 0.14)*
La_2O_3	468	13.0	*(9.85 – 17.33)*	28.5	13.7	*(11.82 – 15.96)*	19.7	*(18.87 – 21.94)*
Ce_2O_3	446	33.3	*(31.65 – 34.84)*	31.4	32.8	*(31.13 – 34.06)*	34.1	*(33.39 – 34.88)*
Pr_2O_3	646	3.72	*(3.05 – 4.33)*	1.75	3.54	*(3.35 – 3.72)*	2.95	*(2.64 – 3.14)*
Nd_2O_3	610	12.8	*(9.52 – 15.51)*	3.97	12.5	*(11.23 – 15.37)*	8.69	*(7.49 – 9.13)*
Sm_2O_3	476	1.61	*(1.04 – 2.32)*	0.19	1.60	*(1.46 – 2.03)*	0.86	*(0.67 – 0.96)*
Gd_2O_3	599	0.87	*(0.48 – 1.22)*	0.25	0.90	*(0.71 – 1.15)*	0.39	*(0.33 – 0.44)*
Tb_2O_3	514	0.07	*(0.00 – 0.10)*	b.d.l	0.05	*(0.04 – 0.06)*	b.d.l	*(0.02 – 0.06)*
Dy_2O_3	517	0.17	*(0.08 – 0.25)*	b.d.l	0.21	*(0.11 – 0.31)*	0.05	*(0.02 – 0.10)*
Er_2O_3	622	0.08	*(0.04 – 0.15)*	b.d.l	b.d.l	*(0.03 – 0.07)*	b.d.l	*(0.00 – 0.03)*
Yb_2O_3	308	b.d.l	*(0.00 – 0.04)*	b.d.l	b.d.l	*(0.01 – 0.03)*	b.d.l	*(0.00 – 0.03)*
CaO	49	0.68	*(0.54 – 0.92)*	0.55	0.56	*(0.32 – 0.97)*	0.41	*(0.36 – 0.47)*
PbO	104	0.00		0.00	0.00		0.00	
Total		99.3		98.2	99.3		99.3	
ΣREY_2O_3		65.9	*(62.62 – 65.97)*	65.9	65.8	*(61.41 – 65.50)*	66.9	*(66.13 – 66.82)*

Aver. = average, Mnz = monazite, Ttn = titanite, Apa = apatite, blank = not analysed, b.d.l. = below detection limit.

Table 6. Composition (in wt%) of xenotime-(Y) from samples K108 and K206.

Sample	K108			K206	
	Det.limit (ppm)	Aver. (n=2)	*Min – Max*	Aver. (n=2)	*Min – Max*
P_2O_5	133	34.1	*(33.98 – 34.20)*	33.2	*(33.10 – 33.20)*
SiO_2	103	0.98	*(0.94 – 1.01)*	1.47	*(1.45 – 1.48)*
TiO_2	265	0.17	*(0.17 – 0.17)*	0.43	*(0.42 – 0.43)*
ZrO_2	194				
ThO_2	53	0.21	*(0.16 – 0.26)*	1.09	*(1.04 – 1.14)*
$UO2$	151	0.08	*(0.05 – 0.10)*	0.24	*(0.17 – 0.31)*
Al_2O_3	94	0.00		0.00	
Y_2O_3	139	42.2	*(42.03 – 42.39)*	42.2	*(41.95 – 42.38)*
La_2O_3	372	0.00		0.00	
Ce_2O_3	342	0.05	*(0.05 – 0.06)*	0.05	*(0.04 – 0.05)*
Pr_2O_3	525	0.09	*(0.08 – 0.11)*	0.07	*(0.07 – 0.08)*
Nd_2O_3	476	0.36	*(0.35 – 0.36)*	0.58	*(0.50 – 0.67)*
Sm_2O_3	405	0.71	*(0.70 – 0.73)*	0.59	*(0.47 – 0.71)*
Gd_2O_3	515	4.55	*(4.47 – 4.63)*	3.49	*(3.46 – 3.52)*
Tb_2O_3	481	0.93	*(0.91 – 0.95)*	0.86	*(0.86 – 0.87)*
Dy_2O_3	469	5.73	*(5.72 – 5.73)*	5.02	*(4.68 – 5.36)*
Ho_2O_3	650	0.86	*(0.85 – 0.87)*	0.79	*(0.78 – 0.80)*
Er_2O_3	559	3.27	*(3.17 – 3.37)*	3.08	*(3.05 – 3.10)*
Tm_2O_3*		0.39	*(0.38 – 0.39)*	0.43	*(0.42 – 0.44)*
Yb_2O_3	280	1.83	*(1.82 – 1.83)*	2.65	*(2.52 – 2.77)*
Lu_2O_3	295	0.29	*(0.28 – 0.29)*	0.41	*(0.40 – 0.42)*
CaO	42	0.06	*(0.06 – 0.06)*	0.03	*(0.02 – 0.03)*
FeO	207	0.00		0.00	
PbO	82	0.00		0.02	*(0.01 – 0.03)*
Total		96.9		96.6	
ΣREY_2O_3		61.3	*(61.14 – 61.37)*	60.2	*(60.08 – 60.29)*

*=interpolated (straight line between nearest adjoining REEs on chondrite normalise plots)